

# Tuning the violins: dark sector phase transition models for the PTA signal

**Torsten Bringmann,<sup>1</sup> Thomas Konstandin,<sup>2</sup> Jonas Matuszak,<sup>3</sup> Kai Schmidt-Hoberg,<sup>2,4</sup> and Carlo Tasillo<sup>5,6</sup>**

<sup>1</sup>*Department of Physics, University of Oslo, Box 1048, N-0316 Oslo, Norway*

<sup>2</sup>*Deutsches Elektronen-Synchrotron DESY, Notkestr. 85, 22607 Hamburg, Germany*

<sup>3</sup>*Institute for Theoretical Particle Physics (TTP), Karlsruhe Institute of Technology (KIT), 76128 Karlsruhe, Germany*

<sup>4</sup>*CP3-Origins, University of Southern Denmark, Campusvej 55, DK-5230 Odense M, Denmark*

<sup>5</sup>*Department of Physics and Astronomy, Uppsala University, Box 516, SE-751 20 Uppsala, Sweden*

<sup>6</sup>*Instituto de Física Corpuscular (IFIC), Universitat de València-CSIC, Parc Científic UV, C/ Catedrático José Beltrán 2, E-46980 Paterna, Spain*

*E-mail:* [torsten.bringmann@fys.uio.no](mailto:torsten.bringmann@fys.uio.no), [thomas.konstandin@desy.de](mailto:thomas.konstandin@desy.de),  
[jonas.matuszak@kit.edu](mailto:jonas.matuszak@kit.edu), [kai.schmidt-hoberg@desy.de](mailto:kai.schmidt-hoberg@desy.de),  
[carlo.tasillo@ific.uv.es](mailto:carlo.tasillo@ific.uv.es)

**ABSTRACT:** First-order phase transitions in a dark sector have been invoked as an intriguing possibility to explain the observed stochastic gravitational wave background at nanohertz frequencies. Here we perform a comprehensive study of the generic requirements for such a phase transition to explain the observed signal while being consistent with all relevant constraints. We consider three broad model classes for strong first-order transitions, realised by an Abelian dark Higgs boson, a two-step phase transition involving two scalar singlets, and a conformal scalar field with loop-induced symmetry breaking, respectively. We discuss the tuning that is required to successfully explain the Pulsar Timing Array (PTA) signal in each of these cases, and highlight the underlying physical mechanisms. We conclude that all three scenarios can in principle describe the data, but that conformal models stand out as the most generic, and least tuned, explanation. Future observations by the PTA collaborations and collider experiments will be crucial to test the viability of this hypothesis, and to further narrow in on the model parameters, if the PTA signal is indeed due to a strong first-order phase transition.

**KEYWORDS:** Phase Transitions in the Early Universe, Early Universe Particle Physics, Cosmology of Theories BSM

ARXIV EPRINT: [DESY-26-014, P3H-26-009, TTP26-002](https://arxiv.org/abs/2602.09092)

---

## Contents

<b>1</b>	<b>Introduction</b>	<b>1</b>
<b>2</b>	<b>Model-independent analysis</b>	<b>3</b>
<b>3</b>	<b>Dark sector phase transition models</b>	<b>7</b>
3.1	Generic correlation between transition strength and speed	8
3.2	Abelian dark sector	10
3.3	Flip-flop	15
3.4	Conformal dark sector	17
<b>4</b>	<b>Confronting models with data</b>	<b>20</b>
<b>5</b>	<b>Discussion of assumptions and caveats</b>	<b>24</b>
<b>6</b>	<b>Conclusions</b>	<b>26</b>
<b>A</b>	<b>Details on the PTArcade likelihood</b>	<b>29</b>
<b>B</b>	<b>Effective potential for the flip-flop model</b>	<b>29</b>
<b>C</b>	<b>Model parameter posterior distributions and benchmark points</b>	<b>30</b>

---

## 1 Introduction

The first observation of gravitational waves (GWs) in 2015 – originating from a binary black hole merger at frequencies of  $\mathcal{O}(100)$  Hz [1] – marked a scientific breakthrough and opened a new window into the Universe. Depending on the astrophysical or cosmological source, gravitational waves can be produced across many orders of magnitude in frequency, motivating a range of complementary experimental strategies [2, 3]. Pulsar timing arrays (PTAs), in particular, are sensitive to very small frequencies in the nanohertz (nHz) regime. In 2020, the NANOGrav collaboration reported evidence for a common red-noise process suggestive of a stochastic nHz gravitational-wave background (GWB) [3]. Subsequent data releases from NANOGrav [4], EPTA & InPTA [5], PPTA [6], CPTA [7], and MPTA [8] confirmed the presence of this signal and also displayed increasing evidence for the characteristic Hellings-Downs correlation associated with a GWB [9]. It is possible that the discovery threshold will already be passed within the upcoming third data release of the International Pulsar Timing Array (IPTA) [10, 11]. This development makes it both compelling and timely to explore potential origins of the GWB signal.

Supermassive black hole binaries (SMBHBs) are astrophysical sources known to contribute to the GWB in this frequency range [3]. However, to match the observed signal

amplitude the local SMBHB number density, merger rates and masses would need to be significantly larger than previously estimated [12–16]; also the predicted power-law spectrum is in some tension with the observed signal shape [17]. In addition, it has been pointed out that the mechanism by which SMBHBs dissipate sufficient energy to come close enough for relevant emission of a GWB is not yet fully understood, a conundrum coined as the ‘final parsec problem’ [18, 19]. It is therefore interesting to consider additional sources of a nHz GWB and it has been widely recognised that there is the exciting possibility that the observed signal may originate from genuinely cosmological sources [20] such as inflation [21], topological defects [22–27], the generation of sub-solar-mass primordial black holes (PBHs)<sup>1</sup> [29–33] or first-order phase transitions (FOPTs) [34–39]. Often these scenarios are specifically tailored to explain the PTA data and it is not always clear how ‘natural’ or realistic the underlying models are.

In this work we will concentrate on the discussion of FOPTs and focus in particular on the question of what is required from the underlying particle physics point of view. The generic requirements on a FOPT to fit the data, while at the same time respecting cosmological constraints, has been laid out in detail in ref. [37]. Specifically, a phase transition capable of generating gravitational waves at nanohertz frequencies must occur at temperatures around the MeV scale. To fit the data the phase transition should furthermore be strong and proceed extremely slowly, resulting in almost Hubble-sized bubbles at percolation. However, new physics at such low energies is already tightly constrained by numerous direct searches [40], which strongly suggests that any such phase transition would have to occur within a largely secluded dark sector. Despite weak couplings to the SM, a dark sector phase transition (DSPT) can still leave observable imprints. In particular, the additional energy density stored in the dark sector can modify the predictions of Big Bang Nucleosynthesis (BBN) and affect the Cosmic Microwave Background (CMB) anisotropies [41–43]. Late decays of dark sector states may also lead to conflicts with BBN or CMB observations [44–48]. Taking into account these constraints, a DSPT could potentially explain the observed signal if (and only if) the dark sector states decay before the time of neutrino decoupling [37].

Here we update the model-independent analysis from ref. [37] to take into account the most recent NANOGrav 15 yr data set, finding that the preferred phase transition parameters shift towards larger temperatures (which generally relaxes constraints from BBN). We study three underlying particle physics models in detail, which are representative of the different qualitative possibilities to satisfy the above requirements, with respectively a

1. thermally induced barrier (as realised in a model with a dark Abelian Higgs boson)
2. two-step phase transition (as realised in a “flip-flop” model, with two scalar singlets)
3. loop-induced barrier (as realised in the conformal version of the dark  $U(1)'$  model).

All these model classes allow a priori for a *strong* FOPT. In all cases, we evaluate in detail what is required for a good fit to the data while simultaneously being in agreement with

---

<sup>1</sup>There is also the possibility that merging primordial SMBHs are responsible for the signal [28].

cosmological and other complementary constraints. Our main conclusion is that while on a model-independent level a FOPT seems to be a generically viable explanation, this conclusion is not generic once the microscopic physics is taken into account. Instead, for both the cases of *(i)* the Abelian dark Higgs and *(ii)* the two-stage phase transition with two singlets, significant parameter tuning is necessary to fit the data. In contrast, for models that are (nearly) conformal, the required parameter space can be realised much more naturally, making this class particularly appealing from a model-building perspective.

This work is organised as follows: In section 2, we present an updated model-independent analysis of the NANOGrav 15 yr data in terms of a DSPT. In section 3, we discuss the three representative particle physics models in detail. In section 4, we confront the models with the PTA data and quantify the required tuning to satisfy all constraints. Section 5 contains a discussion of our results and we conclude in section 6. In three appendices, we provide further details about our PTA likelihood implementation (A), the flip-flop model (B), as well as best-fit points and preferred model parameter ranges for each of the model classes (C).

## 2 Model-independent analysis

In our analysis we will consider the possibility that the GW background at nHz frequencies is dominantly produced by a FOPT in a dark sector. For simplicity, we will typically assume the dark sector to be in thermal equilibrium with the SM bath throughout the transition, but we will also discuss implications of deviating from this assumption. For the scenarios that we are interested in, there are three main phenomenological parameters that determine the shape of the GW spectrum: the transition strength parameter  $\alpha$ , quantifying the amount of vacuum energy released in the transition; the inverse timescale  $\beta/H$  of the transition, determined by the mean bubble separation  $RH_*$  at percolation (both typically stated in units of the Hubble parameter  $H$  at percolation); and the reheating temperature  $T_{\text{reh}}$ , which sets the scale and hence the peak frequency of the GW spectrum. In general, also the bubble wall velocity  $v_w$  impacts both overall spectral shape and peak position of the GW spectrum, but we find  $v_w \approx 1$  in almost all cases of relevance discussed below.

In this section, we will keep the analysis largely model-independent and point out the generic requirements on these phenomenological parameters that must be met in order to provide a good fit to the PTA data. In section 3, we will then turn to the model-building perspective that is the main focus of this article, by discussing the range of dark sector models that could potentially meet the generic requirements outlined here.

Concretely, we will for simplicity consider a situation where the GW production from the DSPT is dominated by sound waves, motivated by the already mentioned fact that we will typically encounter non-runaway bubbles. For these contributions we follow ref. [49] and use the simulation-based [50, 51] template

$$h^2 \Omega_{\text{gw}}^{\text{PT}}(f) = \mathcal{R} h^2 A_{\text{sw}} K^2 \mathcal{Y}_{\text{sw}}(RH_*) \tilde{S}(f), \quad (2.1)$$

for the gravitational wave spectrum. This spectrum takes the form of a doubly broken power law with spectral index 3 at small frequencies ( $f \ll f_1 < f_2$ ) and spectral index  $-3$

at large frequencies ( $f \gg f_2$ ):

$$\tilde{S}(f) = N \left( \frac{f}{f_2} \right)^3 \left[ 1 + \left( \frac{f}{f_1} \right)^2 \right]^{-1} \left[ 1 + \left( \frac{f}{f_2} \right)^4 \right]^{-1}, \quad (2.2)$$

with normalisation  $N = \frac{2\sqrt{2}}{\pi} [(1 + f_2^2/f_1^2) + \sqrt{2}f_2/f_1]$ . The two frequency breaks occur at

$$f_1 \simeq 0.2 \left( \frac{a_* H_*}{RH_*} \right) \quad \text{and} \quad f_2 \simeq 0.5 \Delta_w^{-1} \left( \frac{a_* H_*}{RH_*} \right). \quad (2.3)$$

Here,  $\Delta_w \equiv |v_w - c_s| / \max(v_w, c_s)$  parametrizes the sound shell thickness, with  $c_s$  being the sound speed in the (broken phase) plasma. The mean bubble separation  $RH_*$  at percolation relates to the transition speed as

$$\beta/H = \left( \frac{8\pi}{1 - P_f(T_*)} \right)^{1/3} \frac{\max(c_s, v_w)}{RH_*}, \quad (2.4)$$

where  $P_f(T_*) \approx 0.71$  is the false vacuum fraction at percolation [52, 53]. The red-shifted Hubble rate, finally, is given by

$$a_* H_* = 11.2 \text{ nHz} \left( \frac{T_{\text{reh}}}{100 \text{ MeV}} \right) \left( \frac{g_{\text{reh}}}{10} \right)^{1/2} \left( \frac{10}{h_{\text{reh}}} \right)^{1/3}, \quad (2.5)$$

with  $g_{\text{reh}}$  ( $h_{\text{reh}}$ ) denoting the combined effective number of energy (entropy) degrees of freedom at reheating, in the thermalised SM and dark sector bath. For large values of  $\alpha$ , we expect  $v_w \approx 1$  and hence  $f_1 \sim f_2$ , i.e. almost resulting in a power-law with a single break. For small  $\alpha$ , on the other hand, this is not necessarily the case and the plateau-like intermediate region has to be taken into account for a sufficiently accurate modelling of the GW spectrum; in terms of the concrete models that we discuss further down, this is however only relevant in a small part of the flip-flop model parameter space.

The overall normalization of the spectrum in eq. (2.1) is directly taken from simulations, with  $A_{\text{sw}} \approx 0.11$ , and then further redshifted by a factor of

$$\mathcal{R}h^2 = \left( \frac{a_{\text{reh}}}{a_0} \right)^4 \left( \frac{H_{\text{reh}}}{H_0} \right)^2 h^2 = \Omega_\gamma h^2 \left( \frac{h_0}{h_{\text{reh}}} \right)^{4/3} \frac{g_{\text{reh}}}{g_\gamma}, \quad (2.6)$$

where  $\Omega_\gamma h^2 = 2.473 \cdot 10^{-5}$  is the present energy density in radiation [41],  $g_\gamma = 2$  and  $h_0 = 3.91$ .<sup>2</sup> The signal is also suppressed by a kinetic energy fraction  $K = 0.6\kappa_{\text{sw}}\alpha/(1+\alpha)$ , where we compute the efficiency factor  $\kappa_{\text{sw}} = \kappa_{\text{sw}}(\alpha, v_w)$  following refs. [50, 54]. Finally, we take into account the timescale on which sound waves contribute to the GW signal by introducing the factor  $\mathcal{Y}_{\text{sw}} \equiv \min(1, \tau_{\text{sh}} H_*)$  [55], with  $\tau_{\text{sh}} H_* \simeq RH_* / \sqrt{3K/4}$ .

We now want to compare the generic GW template in eq. (2.1) to the PTA data. For this, we use the PTArcade likelihood [56] of the NANOGrav 15 yr data set [4], taking

<sup>2</sup>For definiteness, we will assume  $g_{\text{DS}} = 2$  light dark sector degrees of freedom in this section, i.e.  $g_{\text{tot}}^{\text{reh}} = g_{\text{SM}}(T_{\text{SM}}^{\text{reh}}) + 2$  and  $h_{\text{tot}}^{\text{reh}} = h_{\text{SM}}(T_{\text{SM}}^{\text{reh}}) + 2$ . We stress that this choice has no noticeable effect on our results in the  $\alpha - \beta/H$  plane because a change in  $g_{\text{DS}}$  can always be absorbed by a small shift in  $T_{\text{reh}}$ .

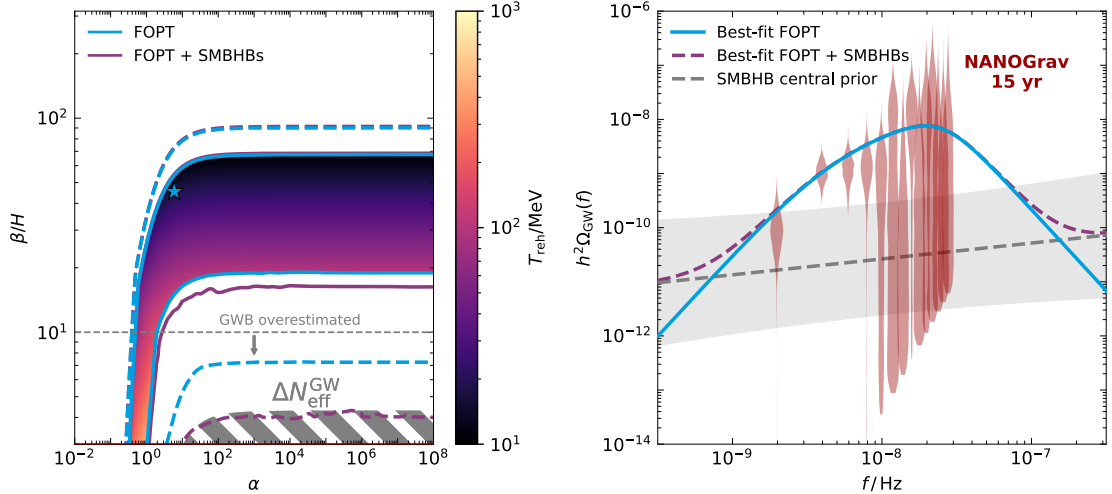


**Figure 1:** *Left panel:*  $1\sigma$  and  $2\sigma$  best-fit regions of current PTA data, interpreted in terms of strength  $\alpha$  and speed  $\beta/H$  of a generic dark sector FOPT (blue lines), with gravitational waves dominantly produced from sound waves due to the expanding bubbles. The colour code shows the corresponding reheating temperature  $T_{\text{reh}}$ , and the hatched grey region indicates the combination of parameters that would generate a total energy density in GWs in conflict with  $\Delta N_{\text{eff}}$  constraints from BBN and CMB [42]. The dashed grey line indicates below which  $\beta/H$  values the computation of the GW signal starts to become unreliable [50] as it is not backed up by simulations. The purple lines indicate the  $1\sigma$  and  $2\sigma$  regions when adding an astrophysical contribution from merging SMBH binaries to the GW signal. *Right panel:* Gravitational wave spectra and NANOGrav 15 yr spectrograms [4] for the best-fit point when allowing both a phase transition and merging SMBH contribution (marked with a blue star in the left panel). The grey area indicates the effect of varying amplitude and slope of the SMBH contribution within their  $1\sigma$  expectation [20].

into account the first 14 Fourier frequencies in the range  $f = [2, 28]$  nHz as recommended by the NANOGrav collaboration [20]. In the left panel of figure 1 we show the results of a profile likelihood analysis in the  $\alpha - \beta/H$  plane, i.e. the iso-likelihood regions after profiling over  $T_{\text{reh}}$  for each point in the plane. The blue solid (dashed) lines indicate the preferred parameter region at the  $1\sigma$  ( $2\sigma$ ) level, respectively. As noted previously [20, 37–39, 57–62], a phase transition interpretation of the PTA data generally requires low  $\beta/H$  and (moderately) large  $\alpha$ , corresponding to slow and strong transitions. The slower the transition, in particular, the less strong it needs to be.

Within the preferred region in the  $\alpha - \beta/H$  plane, we also indicate the corresponding reheating temperatures  $T_{\text{reh}}$  that are needed to explain the data. Ranging from a few 10 MeV to a few 100 MeV, these are higher temperatures than inferred from the NANOGrav 12.5 yr data [37], which relaxes cosmological constraints (see below) significantly. The reason is that the observed signal, see right panel of the figure, is now best fit by the rising part of the phase transition spectrum. Compared to the peak and UV tail of the

GW spectrum, which best described the earlier 12.5 yr data release, this corresponds to a preference for larger peak frequencies and hence larger values of  $T_{\text{reh}}$ .

Let us briefly discuss the impact of two assumptions that we have made in producing figure 1. First, we checked explicitly that even choosing smaller bubble wall velocities  $v_w = 0.7$ , rather than  $v_w \approx 1$  as for the rest of our analysis, only has a minor effect in shifting the allowed contour towards slightly smaller values of  $\beta/H$  in the left panel of the figure. The reason is that the resulting change in normalisation and peak frequency can largely be compensated by adjusting the reheating temperature. Another crucial assumption we have made is thermal equilibrium of dark sector and standard model throughout the transition. The temperature of a secluded dark sector  $T_{\text{DS}}$ , however, may well be different from that of the standard model,  $T$ . We checked that assuming an initially hotter dark sector,  $\xi \equiv T_{\text{DS}}/T > 1$ , has the effect of allowing for slightly smaller values of  $\alpha$ : instead of  $\alpha \gtrsim 0.4$  for  $\xi = 1$ , the left corner of the preferred region extends down to  $\alpha \simeq 0.1$  for  $\xi \simeq 2$  (while increasing  $\xi$  further only has a minimal effect). For  $\xi < 1$ , on the other hand, the rough  $\Omega \propto \xi^4$  scaling (dominantly entering through  $K$  [63]) implies that the small- $\alpha$  solutions visible in the figure will no longer be viable; for  $\xi = 0.5$ , e.g., the allowed parameter space shown in the left panel of figure 1 is restricted to  $\alpha \gtrsim 2$ .

In the discussion so far we have neglected the expected stochastic background from merging SMBH binaries in our analysis [15]. In order to quantify the potential impact of this contribution on our conclusions, we next consider a combined signal of the form  $\Omega_{\text{gw}}(f) = \Omega_{\text{gw}}^{\text{PT}}(f) + \Omega_{\text{gw}}^{\text{BH}}(f)$ . Here, we model  $\Omega_{\text{gw}}^{\text{BH}}$  as a power-law, with amplitude and slope as nuisance parameters that are distributed according to the likelihood implemented in PTArcade [56] (and recommended by the NANOGrav collaboration [20]). We show the  $1\sigma$  and  $2\sigma$  regions resulting from profiling over both  $T_{\text{reh}}$  and the SMBH nuisance parameters as purple lines in the left panel of figure 1. Consistent with earlier findings [20, 37], we thus conclude that the impact is minimal – the main effect being that an additional SMBH contribution generally increases the goodness of fit somewhat, allowing for a somewhat larger range of phase transition parameters to be consistent with the data. The effect is largest for values of  $\beta/H \lesssim 10$ , where the phase transition spectrum peaks at around 100 nHz and the PTA data is mostly fitted by the rising part of the spectrum; the SMBH contribution then helps to accommodate the deviations from a pure power-law shape seen in the data. In the right panel of figure 1 we further illustrate this by showing the best-fit GW spectrum from this combined analysis. The main point is that the slope of  $\Omega_{\text{gw}}^{\text{BH}}(f)$  can only vary between roughly  $-1$  and  $2$ . Even for amplitudes on the high side compared to expectations [15], it is thus difficult to achieve a good fit to the data for more than the first few frequency bins [16]. A phase transition signal, on the other hand, can easily accommodate the large slope seen in the data (combined with a clear prediction of a turnover towards frequencies somewhat larger than currently accessible). In summary, the presence of the astrophysical background is very unlikely to affect conclusions about what is needed for a DSPT to be the dominant cause of the PTA signal, at least given the current knowledge concerning these backgrounds. In the following, we will therefore neglect this contribution to the GW signal and only consider the GWs produced due to the DSPT itself.

Let us finally comment on relevant cosmological constraints for a generic phase transition scenario. First, the GWs produced due to the transition contribute to the radiation content of the universe, potentially in conflict with tight constraints from BBN and CMB that are typically formulated in terms of the number of additional effective neutrino degrees of freedom,  $\Delta N_{\text{eff}} \gtrsim 0.22$  [42]. However, as indicated in figure 1, this constraint is irrelevant inside the parameter region favoured by the PTA signal. Additional light degrees of freedom in the dark sector, on the other hand, are generally a bigger concern. In fact, a phase transition interpretation of the PTA signal can only avoid these constraints if the dark sector completely thermalises with the visible sector before the onset of BBN [37]. Small values of  $\xi$  do not help to evade this conclusion either, because the resulting constraint on  $\Delta N_{\text{eff}}$  is driven by the energy density in the dark sector *after* the transition, which is dominated by the required large amount of liberated energy in the phase transition in order to explain the PTA signal. While we have simply assumed thermal equilibrium in this section, the validity of this assumption will be an important aspect for the discussion of concrete models below.

### 3 Dark sector phase transition models

In the previous section, we outlined the generic requirements on the phenomenological parameters  $\alpha$ ,  $\beta/H$  and  $T_{\text{reh}}$  that are needed in order to allow for a phase transition explanation of the PTA signal. Fundamentally, these quantities follow from the concrete model that realises such a DSPT. In particular, they are all related to the effective potential  $V_{\text{eff}}(\phi, T)$  that results from the underlying theory, with  $\phi$  being the scalar field(s) triggering the PT. The phase-transition strength, to start with, is related to the difference of the pseudo-trace  $\bar{\theta}$  of the energy-momentum tensor in the false and true vacuum, at the temperature  $T_p$  of percolation [64, 65],

$$\alpha = \frac{\bar{\theta}_{\text{false}}(T_p) - \bar{\theta}_{\text{true}}(T_p)}{\rho_{\text{rad}}(T_p)}. \quad (3.1)$$

Here,  $\rho_{\text{rad}}$  is the total energy density in radiation (in the SM and dark sector bath) in the symmetric phase, at the time of percolation, and  $\bar{\theta} \approx (1 - \frac{1}{4}T\partial_T)V_{\text{eff}}(\langle\phi\rangle, T)$  for  $c_s \approx 1/\sqrt{3}$ . For transitions dominantly triggered by thermal (rather than quantum) fluctuations, all other quantities – including  $T_p$  itself – can be derived from the Euclidean bounce action

$$S_3(T) = 4\pi \int r^2 dr \left[ \frac{(\partial_r \bar{\phi}_b)^2}{2} + V_{\text{eff}}(\bar{\phi}_b, T) \right], \quad (3.2)$$

where  $\bar{\phi}_b$  is the bounce solution of the  $O(3)$ -symmetric Klein-Gordon equation for  $\phi$ . This directly translates to the bubble nucleation rate per unit time and volume,  $\Gamma(T) = A(T) \exp(-S_3/T)$ , from which it is in principle straight-forward to calculate the false vacuum fraction  $P_f(T)$  [66]. This, in turn, leads to an implicit definition of  $T_p$  as  $P_f(T_p) = 0.71$  [67] and allows to directly compute the length scale  $RH_*$  [66] which we use for the determination of  $\beta/H$  as in eq. (2.4). In light of the subsequent discussion, we note that a

very useful estimate is often given by

$$\beta/H \approx T \left. \frac{dS_3}{dT} \right|_{T=T_p}, \quad (3.3)$$

a relation which in fact has previously been used as an alternative definition of  $\beta/H$ .

In practice, the computation of the false vacuum fraction  $P_f(T)$  and hence all derived quantities is more involved, as the Hubble rate itself depends on  $P_f(T)$ . This is especially relevant when the vacuum energy released in the transition becomes sizeable. We use the numerical code `TransitionListener` to perform all of the above steps in a self-consistent manner, and refer to ref. [52] for details concerning the implementation.

To illustrate the procedure and to gain some intuition about the expected correlation of  $\alpha$  and  $\beta/H$  in concrete models, we will in the following subsection discuss the case of the thin-wall limit in which the bounce action can be approximated analytically. We will then turn to three concrete DSPT models.

### 3.1 Generic correlation between transition strength and speed

Let us for simplicity consider the following parametric dependence of the potential difference between the true and false vacuum, with constants  $\kappa$  and  $T_c$ :

$$\Delta V = \kappa(T^2 - T_c^2). \quad (3.4)$$

This description is motivated by the leading thermal corrections to the effective potential being proportional to  $T^2$ , and it is designed such that  $\Delta V$  vanishes at the critical temperature  $T_c$ . In a given model, the temperature dependence is more intricate, but this simple form captures the most important features for our discussion.

In the thin-wall limit, i.e. for transitions happening close to criticality  $T_p \lesssim T_c$ , the field profile  $\bar{\phi}(r)$  inside a critical bubble is well-approximated by a step function jumping from the true vacuum to the false one at the bubble radius  $R_0$ :

$$S_3(T) = -2 \times 4\pi \int_0^\infty r^2 dr V(\bar{\phi}(r), T) = \frac{8\pi}{3} \Delta V R_0^3 = 72\pi \frac{\sigma^3}{(\Delta V)^2}. \quad (3.5)$$

Here, the first equality follows from an identity for the bounce solution that relates the gradient field energy to the potential term, similar to the virial theorem in classical mechanics (sometimes called Derrick's or Coleman's trick [68, 69]). In the last step, the critical bubble radius  $R_0 = 3\sigma/\Delta V$  was used to express the bounce action in terms of the wall tension  $\sigma$ . The latter characterises the energy cost of forming the bubble wall due to the height of the potential barrier separating the two minima. In accordance with the thin-wall limit, we will treat  $\sigma$  as being temperature-independent. This is justified since the dependence of the potential barrier on temperature is typically much milder than that of  $\Delta V$ .

Hence, the dominant temperature dependence of the bounce action in our model stems from eq. (3.4), and the transition speed approximation from eq. (3.3) evaluates to

$$\beta/H \approx \frac{S_3(T_p)}{T_p} \frac{T_c^2 - 5T_p^2}{T_p^2 - T_c^2}. \quad (3.6)$$

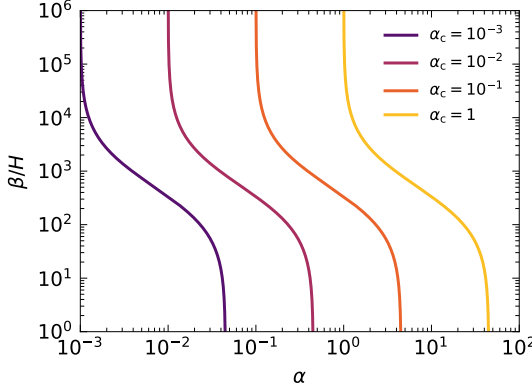


**Figure 2:** Correlation between transition strength  $\alpha$  and speed  $\beta/H$  in the thin-wall approximation for  $S_3(T_p)/T_p = 200$  and different choices of  $\alpha_c$  as introduced in eq. (3.7). See text for details.

We observe that  $\beta/H$  vanishes for a transition happening at  $T_p \rightarrow T_c/\sqrt{5}$  and increases until it diverges for  $T_p \rightarrow T_c$ . The first limit corresponds to metastability, where the bounce action develops a minimum and the phase transition is very slow.

To estimate the phase transition strength parameter  $\alpha$ , we employ eq. (3.1) for a radiation energy density  $\rho_{\text{rad}} = \zeta T_p^4$ , where  $\zeta \equiv \pi^2 g_*/30$  is proportional to the relativistic degrees of freedom  $g_*$  in the thermal bath at temperature  $T_p$ . Assuming for simplicity that  $g_*$  is temperature-independent, we find

$$\alpha = \frac{\kappa}{2\zeta} \frac{(2T_c^2 - T_p^2)}{T_p^4} \equiv \alpha_c \left( 2 - \frac{T_p^2}{T_c^2} \right) \frac{T_c^4}{T_p^4}. \quad (3.7)$$

We hence conclude that lower transition temperatures correspond to stronger transitions: At the critical temperature one finds the value  $\alpha_c = \kappa/(2\zeta T_c^2)$ ; close to metastability,  $T_p \rightarrow T_c/\sqrt{5}$ , the maximum strength is reached at  $\alpha_m = 45 \alpha_c$ .

These relations allow us to predict a strong correlation between  $\alpha$  and  $\beta/H$ , which can be made explicit by eliminating  $T_p$  in eq. (3.6), using eq. (3.7), to obtain

$$\frac{\beta}{H} = \frac{S_3(T_p)}{T_p} \frac{\alpha - 7\alpha_c - 2\sqrt{\alpha_c(8\alpha + \alpha_c)}}{\alpha_c - \alpha}. \quad (3.8)$$

The prefactor  $S_3(T_p)/T_p$  is of order  $\mathcal{O}(200)$  for transitions happening at the MeV scale [70]; the precise value depends on the details of the model like particle content and wall velocity, but plays no role in our estimate. The remaining expression encodes the correlation between  $\alpha$  and  $\beta/H$ : It has a pole at  $\alpha = \alpha_c$  and decreases monotonically to zero at  $\alpha = 45 \alpha_c$ , corresponding to metastability. In figure 2 we show this correlation between  $\alpha$  and  $\beta/H$  for different choices of  $\alpha_c$ , demonstrating that the limit of slow transitions corresponds to strong transitions. However, the figure also clearly illustrates that the generic prediction – i.e. not very close to metastability – are rather fast transitions with  $\beta/H \gg 100$ . In other words, the *generic* expectation from a DSPT is in tension with the requirement to fit the

PTA data that we have identified in the previous section, namely slow and at the same time strong transitions. This is in line with the findings of the following model-specific case studies in sections 3.2–3.4, which illustrate the general difficulties of achieving such slow transitions in concrete models – and possible ways out in near-conformal settings.

Let us conclude by stressing the limitations of the above analytical estimates based on our simplistic model: Most importantly, we relied on the approximate form of the potential difference in eq. (3.4) and the thin-wall limit of the bounce action computation. Both assumptions break down for transitions happening far away from criticality, rendering the above estimates not applicable to a real model for  $\alpha \gg \alpha_c$ . As derived in section 2, it is however precisely this regime of thick walls that is required in order to explain the PTA data. Our analytical estimates thus need to be replaced by numerical computations of the bounce action and the resulting phase transition parameters. In the following subsections, we will demonstrate this explicitly for three concrete and representative DSPT models.

### 3.2 Abelian dark sector

As our first example we consider a dark sector with a  $U(1)'$  gauge symmetry, with associated gauge boson  $A'_\mu$ , and a dark Higgs field  $\Phi$  charged under this symmetry:

$$\mathcal{L} = |D_\mu \Phi|^2 - \frac{1}{4} F'_{\mu\nu} F'^{\mu\nu} - V(\Phi), \quad (3.9)$$

with  $F'_{\mu\nu} = \partial_\mu A'_\nu - \partial_\nu A'_\mu$  and  $D_\mu = \partial_\mu + igA'_\mu$ . The tree-level scalar potential allowing for a minimum at  $\Phi \neq 0$  is

$$V(\Phi) = -\mu^2 \Phi^* \Phi + \lambda (\Phi^* \Phi)^2. \quad (3.10)$$

To study the phase transition dynamics in this model, we compute the finite-temperature effective potential at 1-loop order in perturbation theory. While this is a standard approach in the literature and sufficient for our purposes, we note that higher-order and non-perturbative improvements (e.g., dimensionally reduced effective theories) can reduce gauge and renormalisation-scale dependence and improve the convergence of the expansion [71, 72]. Since our focus is on the qualitative model behaviour and broad parameter trends relevant for the GW signal, we do not expect these refinements to affect our main conclusions, see also the comparison in ref. [73]. The effective potential thus takes the form

$$V_{\text{eff}}(\phi_b, T) = V_0(\phi_b) + V_{\text{CW}}(\phi_b) + V_{\text{ct}}(\phi_b) + V_T(\phi_b, T) + V_{\text{daisy}}(\phi_b, T), \quad (3.11)$$

based on expanding  $\Phi = (\phi_b + \phi + i\varphi)/\sqrt{2}$  around a (homogeneous and static) background field value  $\phi_b$ . Here the first term is the tree-level contribution,  $V_0(\phi_b) = V(\Phi = \phi_b/\sqrt{2})$ , and the second the usual 1-loop Coleman-Weinberg (CW) potential [74],

$$V_{\text{CW}}(\phi_b) = \sum_{a \in \{\phi, \varphi, A'\}} g_a \frac{m_a^4(\phi_b)}{64\pi^2} \left[ \log \frac{m_a^2(\phi_b)}{\Lambda^2} - C_a \right]. \quad (3.12)$$

In this expression, we take the renormalisation scale to be the zero-temperature vev,  $\Lambda = v \equiv \langle \phi_b + \phi \rangle_{T=0} = \langle \phi_b \rangle_{T=0}$ , and we chose on-shell-like renormalisation conditions [75]

enforcing that both vev and background field-dependent masses are given by their classical tree-level expressions, i.e.  $v = \mu/\sqrt{\lambda}$  and

$$m_\phi^2(\phi_b) = -\mu^2 + 3\lambda\phi_b^2, \quad m_\varphi^2(\phi_b) = -\mu^2 + \lambda\phi_b^2, \quad m_{A'}^2(\phi_b) = g^2\phi_b^2. \quad (3.13)$$

This fixes the counterterm contribution  $V_{\text{ct}} = -\delta\mu^2\phi_b^2/2 + \delta\lambda\phi_b^4/4$  in eq. (3.11). The renormalisation scale  $\Lambda = v$  is chosen such that the logarithms in eq. (3.12) are parametrically small for field values around the vev, which is the regime relevant for the phase transition dynamics. Note that this choice would not be appropriate for studying the conformal limit  $\mu \rightarrow 0$ , which we will discuss separately in section 3.4. The internal degrees of freedom are given by  $g_{\phi,\varphi} = 1$ ,  $g_{A'} = 3$  and, since we employ the  $\overline{\text{MS}}$  scheme, the renormalisation constants are  $C_{\phi,\varphi} = \frac{3}{2}$  and  $C_{A'} = \frac{5}{6}$ .

The finite-temperature contribution takes the form

$$V_T(\phi_b) = \frac{T^4}{2\pi^2} \sum_a g_a J_b \left( \frac{m_a^2(\phi_b)}{T^2} \right), \quad (3.14)$$

with the bosonic thermal function  $J_b$  defined in ref. [76]. Infrared divergences in this latter contribution are taken care of by ‘‘daisy resummation’’ [77], for which the Arnold-Espinosa prescription [78] leads to

$$V_{\text{daisy}}(\phi_b) = -\frac{T}{12\pi} \sum_a g_a \left[ (m_a^2(\phi_b) + \Pi_a(T))^{3/2} - (m_a^2(\phi_b))^{3/2} \right]. \quad (3.15)$$

In this last expression the transverse components of  $A'$  are *not* included in the final sum over  $a$ , and the one-loop thermal masses read

$$\Pi_\phi = \Pi_\varphi = \left( \frac{\lambda}{3} + \frac{g^2}{4} \right) T^2, \quad \Pi_{A'_L} = \frac{1}{3} g^2 T^2. \quad (3.16)$$

For sufficiently large couplings  $\tilde{g} \equiv g/\lambda^{1/4} \gtrsim 1$ , this model features a phase transition that turns from cross-over to first order; increasing  $\tilde{g}$  further leads to stronger and stronger supercooling until, for  $\tilde{g} \gtrsim 3$ , a phase transition is prevented by false vacuum trapping [79]. Adding (fermionic) matter fields charged under the  $U(1)'$  implies that slightly larger gauge couplings  $g$  are needed for small values of  $\lambda$ , also to avoid an unstable potential, but otherwise does not change the above picture qualitatively (see ref. [79] for a more detailed discussion).

The above discussion motivates the range of parameters that we are interested in to describe a FOPT at the MeV scale, and which we summarise in the left panel of figure 3. In particular, we choose to scan directly over  $v$  rather than  $\mu$ , as the only dimensionful parameter in the model, given that  $v$  is more directly connected to the scale at which the transition takes place (recalling that  $T_p \sim v$ ). The range of  $\lambda$ , on the other hand, has only limited impact on the phenomenology we are interested in here. In the right panel, we show the resulting range of  $\alpha$  and  $\beta/H$ , along with the mean (log) reheating temperature for each point in this plane. As expected, the ratio  $v/T_{\text{reh}}$  grows with  $\alpha$ , as the phase transition becomes stronger (and more supercooled). For comparison, we also show the results of the

Parameter	Range	Prior
$\tilde{g} \equiv g \lambda^{-\frac{1}{4}}$	$[0.8, 3.2]$	lin
$\lambda$	$[10^{-5}, 1]$	log
$v / \text{MeV}$	$[1, 1000]$	log

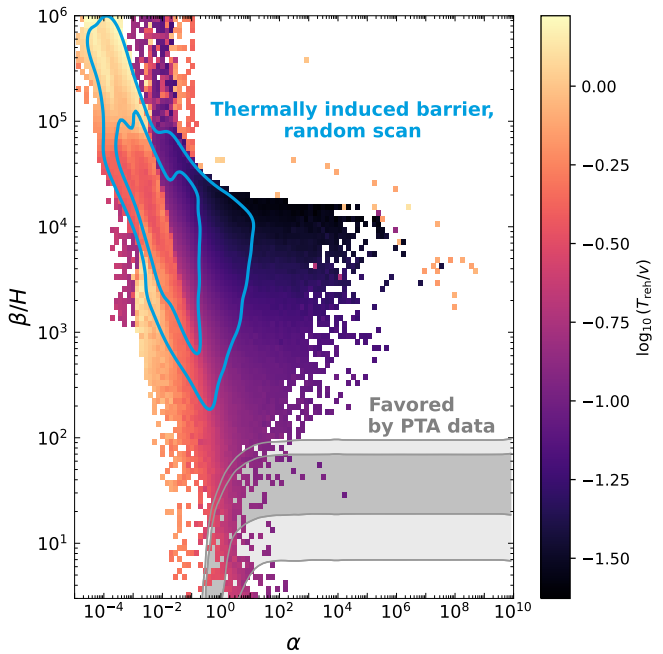


**Figure 3:** *Left panel.* Prior choices for the Abelian dark sector model, targeted at a FOPT at the MeV scale. *Right panel.* The blue lines show the values of  $\alpha$  and  $\beta/H$  for the produced GW signal that correspond – at the  $1\sigma$  and  $2\sigma$  level – to the model parameter ranges in the left panel. For each point in these contours, the colour code indicates the ratio of mean reheating temperature  $T_{\text{reh}}$  and vev  $v$ . For comparison, the grey-shaded area shows the result of the model-independent fit to the PTA data, as displayed in figure 1.

model-independent PTA fit that we discussed in Section 2. Clearly, the generic prediction of the model lies outside the region in the  $\alpha - \beta/H$  plane favoured by the PTA data, with overlap occurring only at (at least) the  $3\sigma$  level. In other words, and as discussed in more detail in Section 4, significant tuning of the model parameters is required to explain the data with a phase transition in an Abelian dark sector.

In figure 4 we illustrate why it is so difficult to identify model parameters that result in GW parameters in the desired regime. The three panels in the top row show the effective potential for three different values of the quartic coupling  $\lambda$  (keeping  $g$  and  $v$  fixed), for a selection of temperatures  $T$ .<sup>3</sup> In general, the potential barrier decreases with temperature, implying a correspondingly smaller tunnelling action and hence more efficient bubble nucleation. A smaller value of  $\lambda$ , as visible when comparing the top panels from left to right, leads to a less rapid decrease of the potential barrier with  $T$  (because the coefficient of the quartic term in the potential only depends logarithmically on the temperature). Bubble nucleation thus becomes less and less rapidly efficient for smaller temperatures and, for very small values of  $\lambda$ , nucleation will in fact become completely inefficient even in the  $T \rightarrow 0$  limit. This is exactly the behaviour that is illustrated in the bottom left panel:

<sup>3</sup>Here we define the false vacuum to correspond to  $V = 0$ , i.e. we subtract  $V_{\text{eff}}(\phi = 0, T)$  from eq. (3.11).

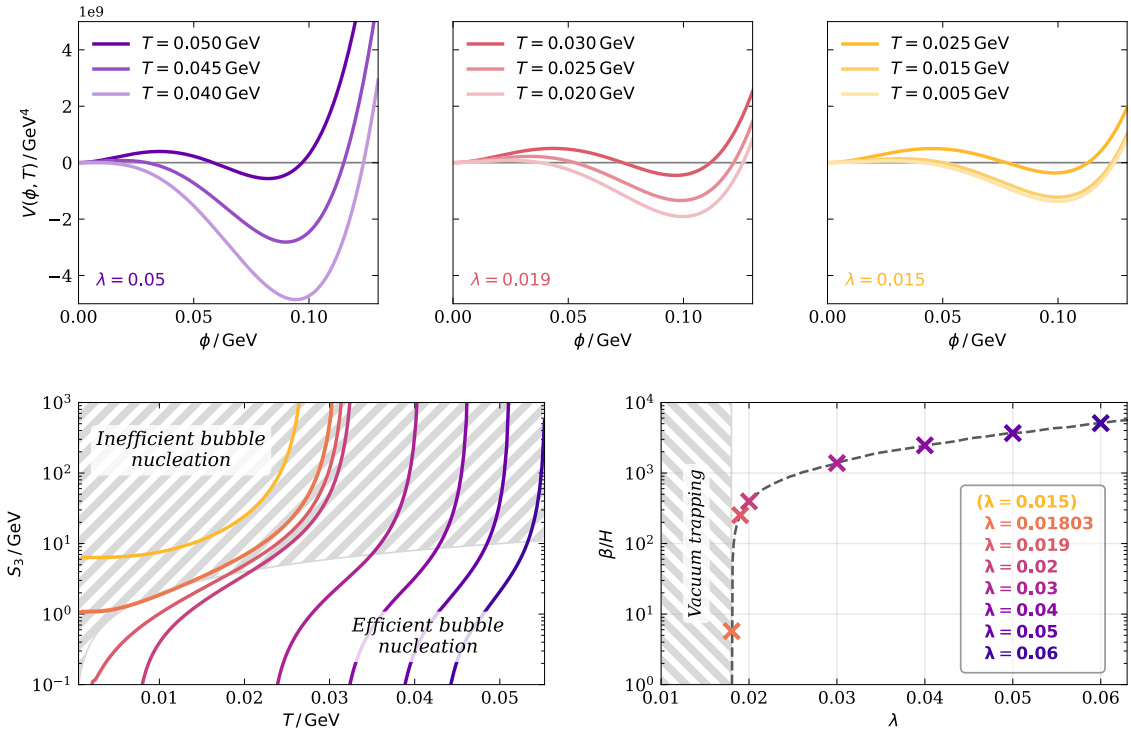


**Figure 4:** *Upper row:* Effective potential of the Abelian dark sector model at different temperatures, choosing for illustration model parameters  $g = 1$ ,  $v = 100$  MeV and three different values of the quartic coupling  $\lambda$  as indicated. *Lower row, left:* Corresponding tunnelling action  $S_3$  as a function of temperature. *Lower row, right:* Resulting inverse transition timescale  $\beta/H$  as a function of the quartic coupling  $\lambda$ .

for small values of  $\lambda$ , the Euclidean action always remains at  $S_3/T > 200$  (indicated as hatched area). Since the transition rate is basically given by the slope of  $S_3/T$ , cf. eq. (3.3), values of  $\beta/H$  that are sufficiently small to explain the PTA data can thus only be achieved for a tiny range of  $\lambda$ . We show this explicitly in the bottom right panel: for values of  $\lambda$  a bit larger than  $\sim 0.018$ , the phase transition proceeds too fast – while for values only slightly smaller, the phase transition does not successfully complete at all. We note that in our parameterisation the necessarily strong tuning that is associated with this observation appears in the quantity  $\tilde{g} \equiv g/\lambda^{1/4}$ , rather than  $\lambda$ , see also the discussion in ref. [80].

So far, we have only discussed the GWs produced by the phase transition, tacitly

assuming that the dark sector temperature equals that of the visible sector. As mentioned in section 2, the dark sector must decay sufficiently quickly afterwards to avoid the stringent BBN constraints on  $\Delta N_{\text{eff}}$ . For the Abelian model, the easiest way to realise this is by assuming the usual portal couplings to be non-vanishing. Specifically, the dark photon (dark Higgs) could decay via kinetic mixing (Higgs mixing) consistent with complementary constraints.

Let us start our discussion with a closer inspection of the produced **dark photons**. We will find later that the preferred dark photon masses in this scenario are in the range  $10 \text{ MeV} \lesssim m_{A'} \lesssim 2 \text{ GeV}$  (see figure 10 in appendix C). This implies that in all cases under consideration electrically charged final states are kinematically available. In order to be compatible with BBN a lifetime  $\tau \lesssim 1 \text{ s}$  is hence required (see ref. [46] for more detailed bounds also taking into account the abundance of the relic). For  $m_{A'} \lesssim 200 \text{ MeV}$ , the main decay channel will be  $A' \rightarrow e^+ e^-$  and  $\tau \lesssim 1 \text{ s}$  corresponds to a kinetic mixing  $\epsilon \gtrsim 10^{-9} - 10^{-10}$ . This is very close to or may even be in conflict with existing supernova limits [81], in particular for masses where cooling in the gain layer is relevant [82]. There is however an open (slightly mass-dependent) window for  $10^{-6} \lesssim \epsilon \lesssim 10^{-4}$  between collider and beam dump limits for  $m_{A'} \gtrsim$  a few MeV. While a viable possibility today, this region may be probed in the near future in particular by Belle II [83], NA64 $\mu$  [84] and LHCb [85], but also by FASER2 [86], DarkQUEST [87] and SHiP [88]. For even heavier dark photon masses,  $m_{A'} \gtrsim 200 \text{ MeV}$ , the bounds become much weaker, as additional decay channels open up (making the decay quicker for fixed kinetic mixing  $\epsilon$ ) while at the same time the dark photons become too heavy to be produced in supernovae.

Turning to the **dark Higgs**, we observe that the preferred masses are somewhat lighter,  $2 \text{ MeV} \lesssim m_\phi \lesssim 1 \text{ GeV}$  (see again figure 10 in appendix C). We also find that for all parameter points of interest  $m_\phi < 2m_{A'}$ , so that the dark Higgs cannot decay into two dark photons. To allow for a consistent phenomenology we therefore need to consider other possibilities, the simplest one corresponding to an induced mixing with the SM Higgs via the usual portal coupling

$$\mathcal{L}_{\text{portal}} = \lambda_{H\Phi} |H|^2 \Phi^* \Phi. \quad (3.17)$$

After electroweak symmetry breaking, such a term would induce a non-vanishing mixing angle  $\sin \theta \simeq \lambda_{H\Phi} \frac{v v_{\text{EW}}}{m_h^2}$  (for  $m_\phi \ll m_h$ ), which would allow for  $\phi$  decays into SM final states. The Higgs portal coupling would also induce an additional effective mass term for  $\phi$  below the electroweak scale, which however can be absorbed into a redefinition of the tree-level parameters without changing the dynamics of the electroweak and dark sector phase transitions. Two separate phase transitions  $(0, 0) \rightarrow (0, v_{\text{EW}}) \rightarrow (v, v_{\text{EW}})$  can be ensured by requiring that the curvature in the  $\phi$  direction of the effective potential remains positive for temperatures around the electroweak scale, i.e.  $\partial_\phi^2 V_{\text{eff}}(h, \phi, T \simeq v_{\text{EW}}) \Big|_{\phi=0} > 0$ . This leads to an upper bound on the portal coupling  $\lambda_{H\Phi} \ll \lambda$ , or equivalently

$$\sin \theta \ll \left( \frac{m_\phi}{m_h} \right)^2 \left( \frac{v_{\text{EW}}}{v} \right) \simeq 10^{-4} \left( \frac{m_\phi}{10 \text{ MeV}} \right)^2 \left( \frac{10 \text{ MeV}}{v} \right), \quad (3.18)$$

where  $m_h = 125$  GeV and  $v_{\text{EW}} = 246$  GeV are the SM Higgs mass and vev, respectively. The analogous condition for the dark sector phase transition to not be affected by electroweak scale physics,  $\partial_h^2 V(h, \phi, T \simeq v)|_{h=v_{\text{EW}}} > 0$ , is then automatically satisfied for  $v \ll v_{\text{EW}}$ . For portal couplings satisfying the bound (3.18), the tree-level mass induced by electroweak symmetry breaking can thus be compensated by a redefinition of the tree-level parameters without affecting the phase transition dynamics. This a posteriori justifies our neglect of the portal coupling in the analysis of the phase transition dynamics.

We find that for the given mass range  $\phi$  decays via Higgs mixing can be efficient enough while respecting current constraints. Specifically, for  $2 \text{ MeV} \lesssim m_\phi \lesssim 2m_\mu$  the allowed range of  $\sin \theta$  is between  $10^{-5} \leq \sin \theta \leq 10^{-4}$ , where the lower bound comes from the requirement that the dark Higgs decays sufficiently early [89] while the upper limit is due to collider and beam dump experiments [90]. Using eq. (3.18) we arrive at the conclusion that this range is consistent with the requirement of two separate phase transitions for almost all of the points shown in figure 3. Once the dark Higgs is sufficiently heavy to decay into muons, cosmological constraints on the mixing angle are significantly relaxed. In particular for masses between the muon and pion threshold values as small as  $\theta \simeq 10^{-9}$  are possible. Overall we therefore find that the minimal addition of kinetic and Higgs mixing is sufficient to make the scenario cosmologically viable without impacting the PT dynamics.

Let us finally remark that the above requirements of a sufficiently fast decay of the DS degrees of freedom automatically guarantees that the dark and visible sector are kept in thermal equilibrium throughout the transition, thus justifying our treatment of assuming  $T_{\text{DS}} = T$  throughout the analysis (for a more detailed discussion see, ref. [79]).

### 3.3 Flip-flop

As our second example, we introduce a two dark singlet model to realize a two-step phase transition. It consists of two real scalars  $\phi_1$  and  $\phi_2$  as well as a Majorana fermion  $\psi = \psi^c$ , which only couples to  $\phi_1$ :

$$\mathcal{L} = \frac{1}{2} (\partial_\mu \phi_1) (\partial^\mu \phi_1) + \frac{1}{2} (\partial_\mu \phi_2) (\partial^\mu \phi_2) + \frac{1}{2} i \bar{\psi} \not{\partial} \psi - \frac{y}{2} \phi_1 \bar{\psi} \psi - V(\phi_1, \phi_2). \quad (3.19)$$

As indicated, we thus assume the bare Majorana masses to be sufficiently small to not affect the phenomenology of the phase transition discussed below. We parametrise the tree-level potential of the two scalars in the suggestive form

$$V(\phi_1, \phi_2) = \frac{\lambda_0}{4} (\phi_1^2 + \gamma^2 \phi_2^2 - v^2)^2 - \frac{\lambda_1}{2} v^2 \phi_1^2 + \frac{\lambda_{12}}{2} \phi_1^2 \phi_2^2. \quad (3.20)$$

The potential is constructed such that its minima,  $(\phi_1, \phi_2) = (\pm \sqrt{1 + \lambda_1/\lambda_0} v, 0)$  and  $(\phi_1, \phi_2) = (0, \pm v/\gamma)$ , are located on the  $\phi_1$ - and  $\phi_2$ -axis, respectively. For  $\lambda_1 > 0$  the minimum in the  $\phi_1$  direction is deeper than the one on the  $\phi_2$ -axis at zero temperature. The coupling  $\lambda_{12}$  between the two scalars creates a tree-level barrier separating the two minima for sufficiently large  $\lambda_{12} > \gamma^2 \lambda_1$ . In order to avoid the phenomenological relevance of domain walls, we further assume some small bias terms, which favour the positive valued minima on both axes, but otherwise do not play any role in our analysis.

We compute the effective potential analogously to the previous section, for more details on the renormalisation and thermal masses see appendix B. The quantum and thermal corrections to the tree-level potential do not push the minima off the two field axes; they merely determine which minimum is the global one at a given temperature, and where on the axes the minima are located. At very high temperatures, the thermal corrections dominate and there is only a single phase at the origin in field space. As the temperature decreases, two scenarios are in principle possible: Either the minimum in the  $\phi_1$  direction appears first, and becomes the global minimum, or the minimum in the  $\phi_2$  direction does so. We are interested in the latter case, which can be achieved by the fermion obtaining a sufficiently large mass  $m_\psi = y\langle\phi_1\rangle/\sqrt{2}$ , depending only on the vev in the  $\phi_1$  direction. That way, the thermal corrections of the phase on the  $\phi_1$ -axis are stronger than those on the  $\phi_2$ -axis. The minimum in the  $\phi_2$  direction then develops first; subsequently, the minimum in the  $\phi_1$  direction changes from a local to the global minimum. If  $\lambda_{12}$  is not too small compared to  $\lambda_0$  and  $\lambda_1$ , the tree-level barrier between the two minima ensures that the second transition step can be supercooled.

The phase structure of such a flip-flop transition is shown for a benchmark point (table 2) in the left panels of figure 5. The right panel shows the effective potential at the nucleation temperature, with the red arrow indicating the tunnelling path. Since the bounce solution lies in the thick wall regime, the release point of the field (end of the arrow) does not coincide with the global minimum of the potential.

The parameter ranges where we search for two-step transitions are summarised in the left panel of figure 6. Note that not all of the points in this parameter space will be physically viable or feature a two-step transition. In our scan, we thus explicitly exclude points where the zero-temperature vacuum is unstable or where the tunnelling action does not drop sufficiently to allow for a successful transition to the global minimum until today, see for reference also the posteriors in figure 11 in appendix C. The right side of figure 6 shows the corresponding range of transition strength  $\alpha$  and speed  $\beta/H$ , with a colour code for the mean (log) reheating temperature at each grid point. It is clear that only a very small fraction of the parameter space gives rise to the  $\alpha$  and  $\beta/H$  values favoured by the PTA data (grey contour). The minima of the first-order transition are in fact further separated in field space than in the case of the Abelian model. This increases the bounce action, suppresses the nucleation rate, and thus leads to smaller  $\alpha$  for similar  $\beta/H$  compared to the dark  $U(1)'$  model from section 3.2.

Just as we discussed in the case of the  $U(1)'$  model, the dark sector has to decay sufficiently quickly to avoid constraints on  $\Delta N_{\text{eff}}$  from BBN. The fermion  $\psi$  is typically the heaviest DS state, and hence strongly Boltzmann suppressed at temperatures  $T \sim m_{\phi_i}$ . In the absence of gauge bosons, the only renormalisable operators are Higgs portal couplings with the scalars as described around eq. (3.17) above. For the case of the two scalars considered here, this slightly generalises to two possible couplings,  $\lambda_{H\phi_i}|H|^2\phi_i^2$ , but the phenomenology is still very similar to the case of the Abelian Higgs described above: After the dark sector transition into the global minimum, the dark singlets can decay via Higgs mixing into electrons (and all other charged final states once the corresponding mass thresholds are crossed), consistent with cosmological and complementary constraints.

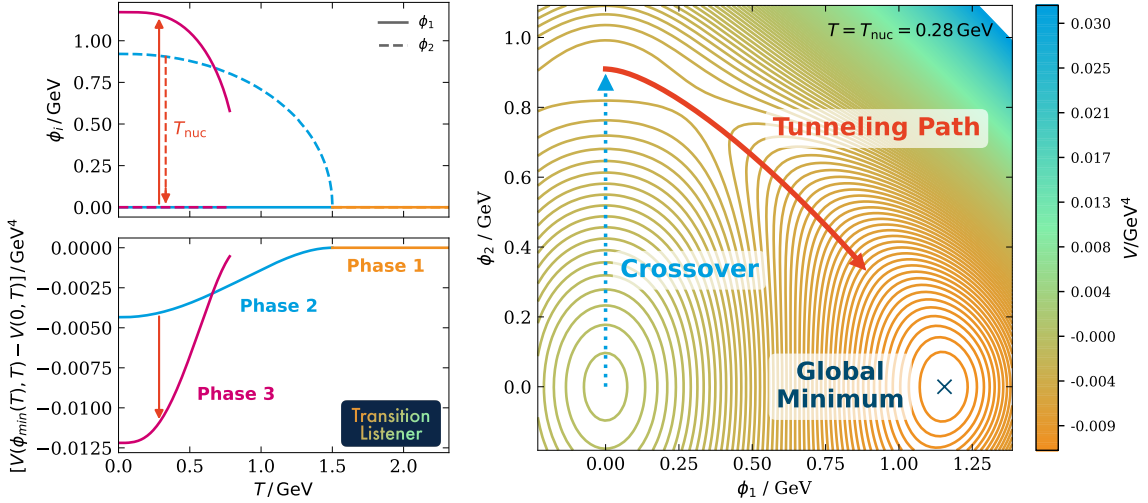


**Figure 5:** *Left panels:* Field values of  $\phi_1$  and  $\phi_2$  as a function of temperature (upper panel) and the corresponding potential values (lower panel). At high temperatures  $T$  the global minimum is at the origin (orange line). At intermediate  $T$  the global potential minimum smoothly shifts from  $(\phi_1, \phi_2) = (0, 0)$  to  $\phi_1 = 0, \phi_2 \neq 0$  with decreasing  $T$  (blue line). At low temperatures, a local minimum at  $\phi_1 \neq 0, \phi_2 = 0$  appears (red line), which eventually becomes the global potential minimum. *Right panel:* Effective potential at the nucleation temperature  $T_{\text{nuc}} = 0.28 \text{ GeV}$ . The blue dotted arrow shows the evolution of the  $\phi_2$  minimum until  $T_{\text{nuc}}$ , the red arrow shows the tunnelling path from the local minimum to the release point of the field. The parameter values for the benchmark point shown are stated in table 2 in the appendix.

### 3.4 Conformal dark sector

As the simplest example of a classically conformal dark sector, we consider the same Lagrangian as in eqs. (3.9, 3.10) but without the dimensionful parameter  $\mu$ , i.e.

$$\mathcal{L} = |D_\mu \Phi|^2 - \frac{1}{4} F'_{\mu\nu} F'^{\mu\nu} - \lambda(\Phi^* \Phi)^2. \quad (3.21)$$

The conformal symmetry of this model is broken at the one-loop level [74], inducing a non-vanishing vev  $v \equiv \langle \phi_b \rangle_{T=0}$ . Taking into consideration the enhanced symmetry, we change the renormalisation condition: Rather than enforcing the tree-level expressions for masses and vev at  $T = 0$ , as in section 3.2, we now demand that the mass of the scalar field  $\phi_b$  vanishes at  $\phi = 0$ , i.e.  $m_\phi^2(\phi_b = 0) = \partial_{\phi_b}^2 V_{\text{eff}}(\phi_b)|_{\phi_b=0} = 0$  in the zero-temperature limit, and

Parameter	Range	Prior
$\lambda_0$	$[10^{-3}, 1]$	log
$\lambda_1$	$[10^{-3}, 1]$	log
$\lambda_{12}$	$[10^{-3}, 1]$	log
$\gamma$	$[0.5, 2]$	log
$y$	$[0.1, \sqrt{4\pi}]$	log
$v / \text{MeV}$	$[10, 10^4]$	log

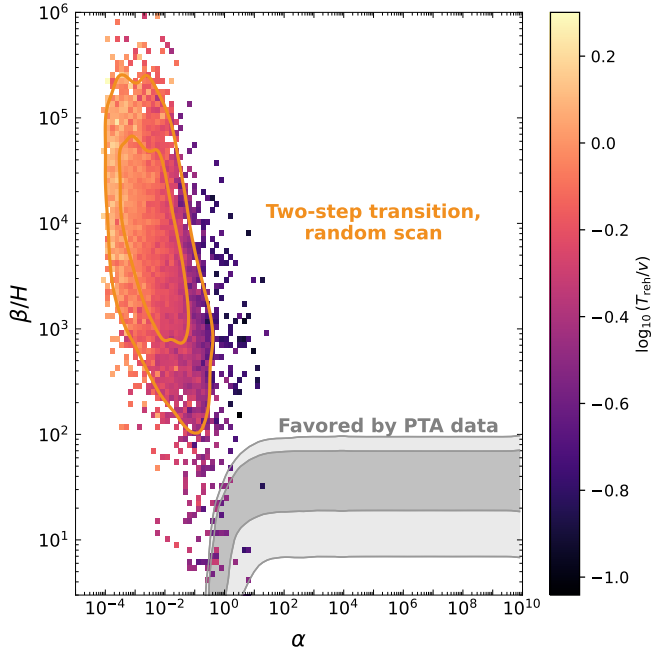


**Figure 6:** *Left panel.* Prior choices for the flip-flop model, targeted at a FOPT at the MeV scale. *Right panel.* Resulting  $1\sigma$  and  $2\sigma$  contours in the  $\alpha - \beta/H$  plane of the produced GW signal, with colour coding indicating  $T_{\text{reh}}$ . For each point in these contours, the colour code shows the ratio of mean reheating temperature  $T_{\text{reh}}$  and vev  $v$ . For comparison, the grey-shaded area corresponds to the result of the model-independent fit to the PTA data, as displayed in figure 1.

define the four-point coupling at some energy scale  $\Lambda$  by requiring  $6\lambda = \partial_{\phi_b}^4 V_{\text{eff}}(\phi_b)|_{\phi_b=\Lambda}$  at  $T \rightarrow 0$ . We take this energy scale to correspond to the (loop-induced) vev,  $\Lambda = v$ , which now differs from the tree-level expression  $v = 0$ . This prescription implies the relation [55]

$$\lambda = \frac{11}{48\pi^2} (10\lambda^2 + 3g^4), \quad (3.22)$$

which determines  $\lambda$  as a function of  $g$ . Similar to the  $U(1)'$  case discussed in section 3.2, adding fermions does not have a significant impact on the phase transition itself; as discussed below, however, it can to some extent help to get rid of the excess energy density and potentially provide a DM candidate [55].

At high temperatures, the term  $T^2\phi^2$  in the  $V_T$  contribution to the effective potential, cf. eq. (3.14), restores the  $U(1)'$  symmetry. In contrast to the  $U(1)'$  model discussed above, however, the barrier now originates from the running of the quartic coupling rather than a thermal cubic term that is produced from gauge bosons. In terms of operators, the running will produce a term of order  $\phi^4 \log(\phi^2)$  which together with the quadratic and quartic terms leads to two local minima in the potential. Since the effect is logarithmic, the scalar field

Parameter	Range	Prior
$g$	$[0.5, 2]$	linear
$v$	$[1, 1000]$ MeV	logarithmic

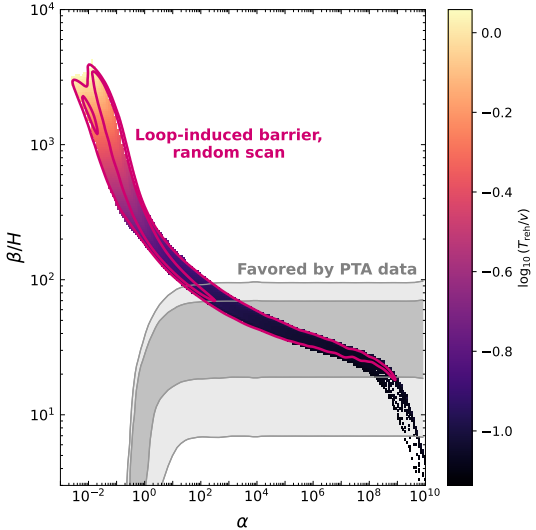


**Figure 7:** *Left panel.* Prior choices for the conformal dark sector model, at the MeV scale. *Right panel.* Resulting  $1\sigma$  and  $2\sigma$  contours in the  $\alpha - \beta/H$  plane of the produced GW signal, with colour coding indicating  $T_{\text{reh}}$ . For each point in these contours, the colour code shows the ratio of mean reheating temperature  $T_{\text{reh}}$  and vev  $v$ . For comparison, the grey-shaded area corresponds to the result of the model-independent fit to the PTA data, as displayed in figure 1.

value at the maximum of the barrier is typically much smaller than the scalar vev in the global minimum. This leads to lower phase transition temperatures and hence stronger phase transitions, see also ref. [91]. For sufficiently large gauge couplings  $g$  the running of  $\lambda$  is sizeable and the conformal model will thus always result in a FOPT.

We summarise the corresponding range of parameters that are potentially interesting for a FOPT at the MeV scale in the left panel of figure 7. For values of  $g \gtrsim 0.5$  the model allows for first-order phase transitions; for lower values of  $g$ , the transition does not succeed ( $P_f < 0.01$ ) until today due to vacuum trapping. The transition becomes weaker and proceeds more quickly as  $g$  grows, up to roughly  $g \approx 2$ , beyond which the quadratic relation (3.22) for  $\lambda$  admits no real solution and perturbation theory breaks down. In the right panel of figure 7 we show the values of  $\alpha$  and  $\beta/H$  that result from a random scan over these parameter ranges, with the  $1\sigma$  and  $2\sigma$  contours indicated by red lines. We observe a clear anti-correlation between  $\alpha$  and  $\beta/H$ , similar to the one expected from the analytical arguments presented in section 3.1. A significant fraction of the resulting phase transitions are strong enough ( $10^2 \lesssim \alpha \lesssim 10^8$ ) and sufficiently slow ( $20 \lesssim \beta/H \lesssim 100$ ) to lie in the region favoured by the PTA data. As in the previous two examples, the reheating temperature after the phase transition is typically of order a few hundred MeV and consistent with the expectations that  $T_{\text{reh}}/v$  drops for stronger transitions.

The decay of the dark sector prior to BBN is again a necessary requirement in order to

avoid stringent constraints on  $\Delta N_{\text{eff}}$ . In principle, the same decay channels as discussed in section 3.2 could be employed to achieve this. In contrast to the other cases, however, in the conformal scenario couplings to the SM cannot easily be realised via a Higgs portal interaction due to the associated induced effective mass below the electroweak symmetry breaking scale: a non-zero portal coupling would violate the assumption of near-conformality and thus significantly modify the phase transition dynamics. While this may result in a viable phenomenology, we do not consider this possibility here and restrict our discussion to the near-conformal framework.

We find that some additions to the minimal conformal model are required to achieve a scenario consistent with cosmological constraints. The arguably simplest solution would be to add a second Abelian gauge group  $U(1)'_2$  that  $\phi$  is charged under and that mixes kinetically with  $U(1)_{\text{EM}}$ , but with a significantly smaller gauge coupling  $g_2 \ll g$ . We checked that for a large range of gauge couplings  $g_2$  this will not significantly change the PT dynamics, while allowing the dark photons  $A'_2$  to be still sufficiently heavy for decays  $A'_2 \rightarrow e^+ e^-$  via kinetic mixing. The DS can then efficiently transfer its energy density to the SM via dark Higgs decays  $\phi \rightarrow A'_2 A'_2$  followed by  $A'_2 \rightarrow e^+ e^-$ , thereby guaranteeing a consistent cosmological setup. Other possibilities that allow the dark sector to decay sufficiently quickly before BBN have been discussed in refs. [38, 55].

## 4 Confronting models with data

In the previous section, we have discussed at length the three sample models that we considered as possible representatives of the type of broader model classes that may explain the GW signal observed by PTAs. The generic GW predictions of these models, in particular, were shown in figures 3, 6 and 7. For ease of comparison, we combine them in the left panel of figure 8 in the  $\alpha - \beta/H$  plane, along with the results of the model-independent analysis of the PTA data presented in Section 2. Already a quick glance at this figure indicates that it should indeed be straight-forward to explain the PTA signal in terms of a phase transition that results from the breaking of a conformal symmetry, with a loop-induced barrier, while it will be significantly more challenging to achieve the same for the other options, based on a thermally induced barrier and a two-step transition, respectively.

In order to test this expectation, we next sample over the full PTA likelihood described in Section 2. Due to the `PTArcade` implementation of the PTA likelihood being unphysical below a certain threshold, we extend this likelihood to a function that smoothly approaches the `PTArcade` likelihood in the region of interest, while driving the `ultranest` [92] sampler away from uninteresting likelihood plateau regions. In view of the numerically highly challenging sampling procedure, we further adopt our strategy to identify parameters with a good fit to the PTA data. For the Abelian dark Higgs model, this means that we only scan over the restricted range  $10^{-3} \leq \lambda \leq 1$ . In the case of the two-step model, we fix  $y = \gamma = 1$  and sample only over the remaining four parameters; for this setup, we start with an initial `ultranest` scan and then use the 100 (unconverged) samples with the highest likelihood to initialise an MCMC sampler.

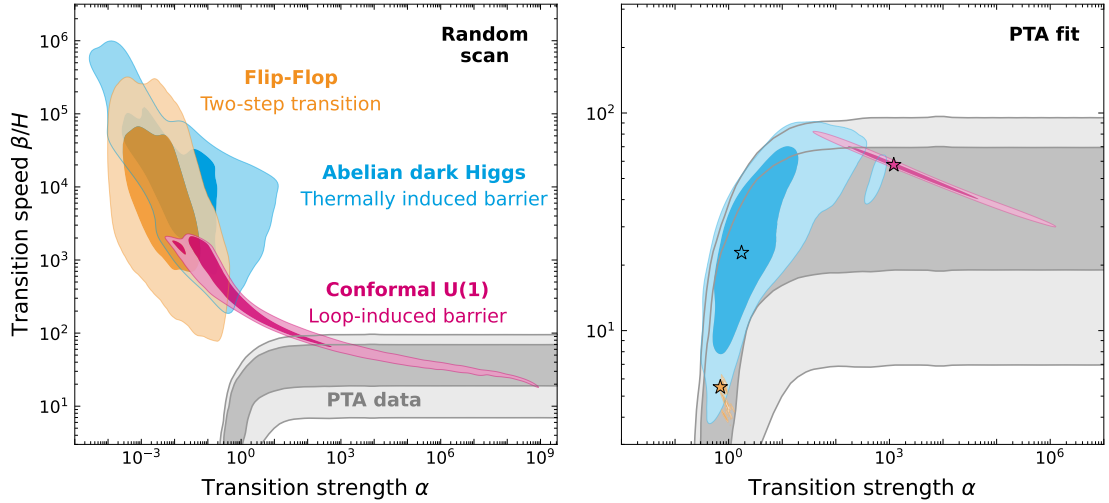


**Figure 8:** *Left panel:* Generic predictions of our three sample models in the  $\alpha - \beta/H$  plane (coloured areas), as displayed earlier in figures 3, 6 and 7. For comparison, the grey-shaded area shows the results for the model-independent fit to the PTA data, cf. figure 1. *Right panel:* Preferred regions for the same models after sampling over the PTA likelihood, with stars indicating the respective best-fit points (cf. tables 2 and 3 in appendix C). Note that the contours in the right panel are only indicative for the Abelian Higgs and the flip-flop model, see also footnote 4, and that the different models require very different amounts of tuning to explain the PTA data, see the discussion around table 1.

In all cases, we further exclude parameter points that do not lead to a successful phase transition, i.e. where nucleation or percolation or  $P_f < 0.01$  would not happen before today, or have tachyonic modes in the zero-temperature vacuum state. Further, we reject points of the two-step model which have scalar masses below the muon threshold after the transition, in order to allow for sufficiently fast decays of the dark sector before BBN without the need of adding large bare mass terms, as discussed in section 3.3. For details on the adopted PTArade likelihood and the resulting posterior distributions of the model parameters see appendices A and C, respectively.

We show the resulting best-fit regions in the right panel of figure 8, with  $1\sigma$  and  $2\sigma$  contours<sup>4</sup> relative to the respective best-fit points (represented by stars; see table 2 in the appendix for the corresponding model parameter values). These best-fit points indeed all describe the data equally well, as indicated by very similar likelihoods of  $\ln \mathcal{L} = -103.28$

<sup>4</sup> Due to the substantial numerical cost of the sampling, in particular for the Abelian dark Higgs and flip-flop models, we deliberately terminated the sampling before full convergence was reached. We note that these sampling challenges are directly related to the tuning issues discussed further down. Extending the chains further would somewhat refine the detailed contour shapes, in particular, but not affect the location of the best-fit points. While the qualitative shape of the confidence regions shown in the figure should thus only be regarded as indicative, this has no impact on our qualitative conclusions – and hence does not warrant additional computational effort.

Conformal model		Abelian dark sector			
$-v^2 \frac{d^2}{dv^2} \ln \mathcal{L}$	$-g^2 \frac{d^2}{dg^2} \ln \mathcal{L}$				
$7 \times 10^1$	$5 \times 10^3$				
Flip-flop					
$-v^2 \frac{d^2}{dv^2} \ln \mathcal{L}$	$-\lambda_0^2 \frac{d^2}{d\lambda_0^2} \ln \mathcal{L}$	$-\lambda_{12}^2 \frac{d^2}{d\lambda_{12}^2} \ln \mathcal{L}$	$-y^2 \frac{d^2}{dy^2} \ln \mathcal{L}$	$-\lambda_1^2 \frac{d^2}{d\lambda_1^2} \ln \mathcal{L}$	$-\gamma^2 \frac{d^2}{d\gamma^2} \ln \mathcal{L}$
$9 \times 10^2$	$3 \times 10^6$	$2 \times 10^7$	$2 \times 10^7$	$5 \times 10^7$	$2 \times 10^8$

**Table 1:** The second derivative of  $\ln \mathcal{L}$  with respect to the model parameters, for the best-fit points indicated with stars in the right panel of figure 8 (cf. tables 2 and 3 in appendix C). See text for a more detailed discussion of how these numbers relate to the relative parameter tuning that is needed to explain the PTA signal in these models.

( $-103.21, -103.42$ ) for the pink (blue, orange) star.

The PTA best-fit regions shown in the right panel of figure 8 only overlap with the generic predictions (left panel) in the case of the conformal model, despite almost identical likelihoods, and are significantly displaced for the other two models. This indicates that in the latter cases some tuning of the underlying model parameters is needed in order to explain the PTA signal. In order to gain some intuition about how this statement may be quantified, we consider the respective best-fit points and compute the second derivative of the likelihood in the direction of each model parameter. The result is shown in Table 1, confirming the general expectation from the discussion above: the same change in  $\ln \mathcal{L}$  requires a much larger change in the coupling  $g$  of the conformal model compared to any of the coupling parameters appearing in the other two models. Let us stress that while  $\left(-g^2 \frac{d^2}{dg^2} \ln \mathcal{L}\right)^{-1/2}$  is a good indicator of the *relative* amount of tuning that is needed close to the respective best-fit points, in comparison between these models, it cannot be used to quantify this tuning in absolute terms. For the latter, one would rather be interested in the same quantity for the *profiled* likelihood, which follows a  $\chi^2$  distribution for any given parameter. An even more reliable estimator is the range of the respective model parameter within a given confidence interval, as computed from the profiled likelihood. Due to the associated computational costs of fully profiling over all (other) model parameters, we only performed this exercise for the conformal model. Profiling over  $v$ , we thus find that  $g$  can vary by roughly 15 % at the  $2\sigma$  level – indicating that, indeed, only a very moderate amount of tuning is needed to fit the data in this case. We note that the significant tuning required for the *other* models also explains the numerical challenges in precisely mapping out the confidence levels in these cases, which we mentioned in footnote 4. It is worth remarking that the dependence on the relevant energy scale, which we parameterised in terms of the vev  $v$ , is quite weak in all models. This is due to the fact that changing  $v$  merely shifts the peak frequency of the GW signal, which can be compensated by a change

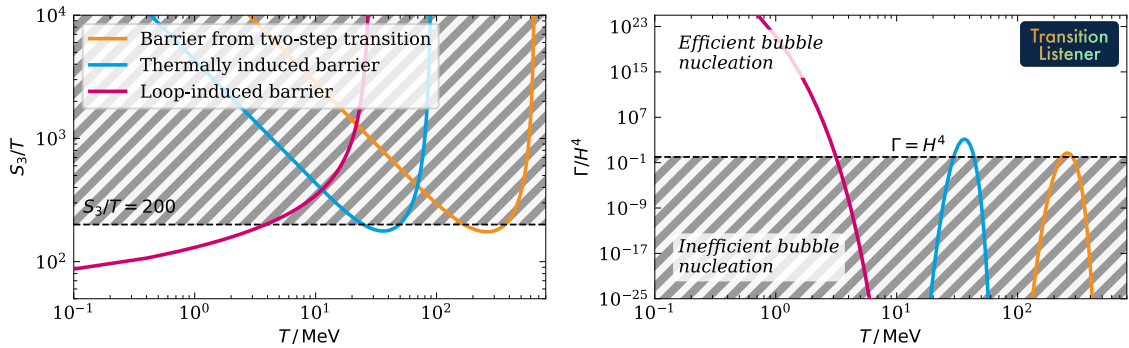


**Figure 9:** Comparison of the tunnelling action  $S_3/T$  (left) and transition rate  $\Gamma/H^4$  (right) as a function of temperature, for the three benchmark models defined in table 2 (and indicated as stars in figure 8).

in  $\beta/H$  to achieve a similar fit to the data. This can also be seen by comparing the width of the posterior distributions in  $v$  in figures 10, 11 and 12, in appendix C with the width of the posterior distributions for the couplings in the respective models.

We stress that the above discussion about the required tuning of model parameters does not strongly depend on the specific parameterisation that we have chosen. Rather, it is a direct consequence of the different physical behaviours of the models considered here, based on how the phase transition proceeds. We illustrate this point in figure 9, by showing the bounce action (left panel) and bubble nucleation rate (right panel) for the three best-fit points discussed above. As already anticipated from the discussion in section 3.2, cf. figure 4, the bounce action of Abelian models with  $\mu^2 \neq 0$  that fits the PTA data is U-shaped. This is expected because it is the only way of flattening  $S_3/T$  sufficiently around  $S_3/T \simeq 200$  to allow a slow PT, and in particular avoiding the rapid formation of bubbles significantly smaller than the original Hubble patch. For the flip-flop model the situation is similar, though we generally find higher  $T_p$  and lower  $\alpha$  because less supercooling is necessary to produce a strong signal. Still, fine-tuning is needed to obtain small transition rates  $\beta/H$ , i.e. an approximately flat  $S_3/T$  just outside the hatched area indicating inefficient bubble nucleation. In contrast, no fine-tuning is needed in the conformal model because, as a consequence of the logarithmic temperature dependence of the potential barrier, the transition automatically sets in at a low temperature. Here  $S_3/T$  only acquires its minimum for  $T \rightarrow 0$  and is therefore always sufficiently flat around  $S_3/T \simeq 200$  to guarantee a small  $\beta/H$ , without fine-tuning. We take the qualitatively

different behaviour of the curves in figure 9 as indication that the models we have studied here are indeed representative of three rather generic model classes that may be invoked as phase transition interpretations of the PTA data.

We complement the above discussion with a more detailed view of the underlying model parameters in appendix C, where we show posterior distributions in the form of triangle plots for each scenario after sampling over the PTA likelihood. These plots make explicit which combinations of couplings and mass spectra are preferred once the PTA fit requirement is imposed, and they provide a useful cross-check of the qualitative tuning arguments discussed around table 1. In particular, they illustrate that the conformal model achieves a good fit in a comparatively broad region of its two-dimensional parameter space, whereas the Abelian Higgs and flip-flop scenarios only populate narrow ridges or isolated patches of parameter space consistent with the data. We also include posterior distributions of the derived particle masses after the phase transition in these triangle plots, which we already referred to in section 3 when discussing possible decay channels and cosmological constraints. In general, we find that these distributions are much stronger peaked than the corresponding prior distributions, indicating the exciting prospect that improved GW data might in principle be used to ‘measure’ the masses of particles that remain inaccessible to direct laboratory searches. Since the couplings are in all cases relatively sharply peaked, the widths of the mass distributions mostly reflect the widths of the posterior distributions of the vevs  $v$ . In accordance with what is visible in figure 9, the conformal model generally favours the smallest vev (peaking around  $\sim 200$  MeV) while the flip-flop model requires significantly larger vevs (peaking around  $\sim 1$  GeV). Correspondingly, both Abelian Higgs and conformal model typically feature scalar masses of  $\mathcal{O}(10)$  MeV, while the lighter scalar mass in the flip-flop model peaks at several hundred MeV. We note that this difference is at least partially driven by our hard cut of  $m_{\phi_i} > 2m_\mu$  in the latter case.

## 5 Discussion of assumptions and caveats

In this section we discuss various assumptions that went into our analysis and comment on possible caveats and extensions of our work. We start with effects that may (moderately) shift the preferred regions in the  $\alpha - \beta/H$  plane, discuss other model classes than those considered above and then turn to potentially critical issues.

**Ultraslow transitions, PBHs, and GW spectral templates:** In figure 1 we indicated that for  $\beta/H \lesssim 10$  our results become less reliable, because both the GW modelling and the transition dynamics enter a regime not well covered by existing simulations. First, the simulation-based scaling of the GW amplitude with  $\beta/H$  used in eq. (2.1) has not been validated for ultraslow transitions, and Hubble expansion effects may lead to an additional suppression of the GW signal [93]; if confirmed, this would shift the preferred region towards smaller  $\beta/H$ . Second, ultraslow transitions with almost Hubble-sized bubbles have been argued to lead to the formation of a large abundance of primordial black holes (PBHs) and an additional, scalar-induced GW component [94–96]. Recent works, however, have questioned these claims, highlighting the importance of a gauge-independent treatment of

the curvature perturbations [97, 98]. Moreover, the common assumption of a nucleation rate that is exponential in time can fail in precisely the ultraslow regime (cf. figure 9), making quantitative PBH estimates model-dependent. Finally, our GW spectral template is based on the latest “Higgsless” sound-wave simulations [50, 51], formally validated up to  $\alpha \lesssim 0.5$ . For  $\alpha \gg 1$  the spectrum is however expected to approach a single-broken power law as in ref. [99] (used in the current LISA pipeline [49]), with differences in the low-frequency slope and amplitude scaling. Given the lack of simulations interpolating between these regimes, we do not attempt to fold these effects into the likelihood. Importantly, any such refinements would predominantly affect the very small- $\beta/H$  region and thus mainly the (already strongly tuned) two-step case; we therefore do not expect our main conclusions to change.

**Energy budget time dependence:** In our sound-wave prediction we follow the common choice of evaluating  $\kappa_{\text{sw}}$  at percolation [100]. For intermediate strengths this can matter because  $\alpha$  (and hence  $\kappa_{\text{sw}}$ ) is typically smaller at nucleation than at percolation, potentially reducing the predicted GW amplitude by up to  $\mathcal{O}(10^2)$  in extreme cases if  $\kappa_{\text{sw}}$  is evaluated too early. These points would hence not yield a good fit to the PTA signal and would need to be shifted towards slightly higher  $\alpha$ . For  $\alpha \gg 1$  this sensitivity is mild since  $\kappa_{\text{sw}} \approx 1$  at both nucleation and percolation. A more faithful treatment would require capturing the time dependence of the energy budget seen in recent simulations [51]. The only model where this could affect the exact location of the best-fit region is again the two-step case, where intermediate strengths in the PTA fit are common.

**Alternative model mechanisms:** We focussed on thermal transitions in weakly coupled scalar sectors, but other mechanisms might modify or even bypass the  $\alpha - \beta/H$  correlations. Non-thermal (quantum) phase transitions can yield parametrically small transition speeds  $\beta/H$  because the nucleation rate is not temperature-dependent; explicit PTA-motivated examples exist [101], with general expectations discussed in [102]. Seeded decay by topological defects (domain walls/cosmic strings) can enhance nucleation and set the bubble scale by defect separations, potentially allowing higher transition temperatures while keeping PTA-scale peak frequencies [103–107]. In our flip-flop model, such effects could in principle arise due to the first transition step generating domain walls, which we however assumed to vanish sufficiently quickly to not have a phenomenological impact. Finally, strongly coupled confining sectors often feature only limited supercooling, resulting in a suppressed GW signal. This expectation has been emphasised recently [108], with large- $N$  pure Yang–Mills being a classic example [109]. A notable exception are near-conformal strongly coupled transitions, whose GW phenomenology we expect to be qualitatively similar to the conformal scenario discussed in section 3.4. Further work would be needed to robustly establish this conclusion, cf. ref. [60] for a first step in this direction.

**Homogenisation before BBN:** It has been argued that strong first-order phase transitions can produce large-scale inhomogeneities that may survive until BBN and spoil the successful nucleosynthesis predictions [43]. In our MeV-scale setting, the concern could be even more acute due to the shorter time available for homogenisation. However, ex-

isting estimates rely on simplified homogenisation dynamics (i.e., baryon diffusion as the dominant effect), whereas strong FOPTs generically also generate bulk flows and turbulence that may accelerate homogenisation. Given these uncertainties, we do not attempt to include homogenisation constraints here. It should be noted, however, that these effects would predominantly affect the very strong transition regime relevant for the conformal model, and we therefore cannot exclude that they may impact our conclusions in this case.

In summary, even though various assumptions and caveats in principle apply to our analysis, we do not expect them to significantly affect our main conclusions. Both the selected model classes and our treatment of the generated GW spectrum, in other words, can thus be understood as representative of rather generic possibilities to explain the PTA signal in terms of a first-order phase transition in a dark sector. Still, future work is needed to address some of the discussed issues in more detail, especially in the case of ultraslow transitions, in order to fully exploit the potential of PTA observations to probe the dynamics of first-order phase transitions in the early universe.

## 6 Conclusions

The recent observation of a common red noise signal by various PTA collaborations offers a new probe of strong dynamics in the early universe through the associated stochastic gravitational wave background. A particularly interesting possibility is that this signal originates from a dark sector first-order phase transition at temperatures around the MeV scale. In this work we have scrutinised the viability of this explanation. In the first part (section 2), we therefore started by performing a model-independent analysis of the 15 yr PTA data to infer the preferred regions in the parameter space spanned by transition strength  $\alpha$ , speed  $\beta/H$  and reheating temperature  $T_{\text{reh}}$  of the phase transition. We thereby updated earlier results based on previous data releases, cf. figure 1, confirming that a phase transition interpretation of the data requires a transition that is both rather strong and slow.

In the remainder of our work, we then studied three representative model classes that can give rise to a first-order phase transition consistent with these observations. These model classes are based on (i) a thermally induced barrier in a higgsed Abelian dark sector, (ii) a two-step ‘flip-flop’ transition in a model with two scalar singlets, and (iii) a loop-induced barrier in an Abelian dark sector that is classically conformally invariant. Among these, we conclude that only the conformal model can explain the PTA signal without significant tuning requirements for the model parameters. We stress that this result is rather generic and can be traced back to the different physical behaviours of the models, based on how the phase transition proceeds (cf. figures 8 and 9):

- In the case of a thermally induced barrier, a moderate amount of supercooling is needed to fit the PTA data and the nucleation rate must be significantly tuned to achieve slow transitions  $20 \lesssim \beta/H \lesssim 100$ . The intrinsic reason for this tuning is that the bubble nucleation rate has to peak at sufficiently low temperatures to

achieve strong supercooling, while at the same time being sufficiently flat around the percolation temperature to guarantee a slow transition.

- Somewhat less supercooling,  $\alpha \sim 1$ , is required in the case of a two-step transition; in this case, however, the transition speed must be tuned down to  $\beta/H \lesssim 10$  in order to explain the PTA signal, stretching the validity of the employed GW spectral templates. The large amount of tuning is again due to the need of flattening the bubble nucleation rate around the percolation temperature. Crucially, the presence of an additional field direction in which tunnelling can proceed typically suppresses the bounce action and enhances the bubble nucleation rate.
- In contrast, the conformal model naturally leads to strong supercooling and slow transitions, such that for  $10^1 \lesssim \alpha \lesssim 10^6$  and  $30 \lesssim \beta/H \lesssim 100$  the PTA signal can be explained without any significant tuning of the model parameters. The reason for this behaviour is the weak temperature dependence of the potential barrier, which automatically leads to a transition at low temperatures after strong supercooling: Here, the bounce action  $S_3/T$  only acquires its minimum for  $T \rightarrow 0$  and is therefore always sufficiently flat around percolation to guarantee a slow transition.

In our analysis we discussed various ways in which additional constraints from BBN and CMB observations, as well as collider searches for light new particles, may be avoided. Most importantly, we find that while the GWs themselves result in a negligible contribution to  $\Delta N_{\text{eff}}$ , the same does not hold for the additional light degrees of freedom in the dark sector after the transition. Generally speaking, those contributions to  $\Delta N_{\text{eff}}$  can be prevented by allowing scalar or gauge boson decays into SM particles before BBN, or by introducing additional dark sector states that help in thermalising the dark sector with the SM. Whether these options are viable is a model-dependent question that we comment on in some detail for each of the scenarios studied here. We also discuss various potential caveats and possible further refinements of our analysis, but argue that none of those affects our main conclusion. All three model classes considered here can thus indeed be seen as representative of rather generic possibilities to explain the PTA signal in terms of a first-order phase transition in a dark sector. In particular, it appears challenging to address the tuning issues without a potential barrier that is only radiatively induced, though it should be noted that in that case complementary constraints are more difficult to avoid.

Further work will be beneficial to address some of the discussed assumptions and caveats in more detail once even more precise PTA data become available. This is expected to happen already in the near future, with the third IPTA data release [10] as well as in upcoming data releases of the individual PTA collaborations. After having confirmed the gravitational wave nature of the observed common red noise signal, in particular, the most important next steps will be to determine its spectral shape more precisely, and whether the signal is isotropic [110, 111]. This will make it possible to better discriminate between different sources, including first-order phase transitions and supermassive black hole binaries. Should a first-order phase transition remain a plausible option, upcoming data will also shrink the preferred regions in the generic  $\alpha - \beta/H - T_{\text{reh}}$  parameter space,

which in turn will help to further discriminate between different model classes. Our work provides a first step in this direction, by identifying already at this stage which model classes appear to most naturally explain the observed signal.

## Acknowledgments

We thank Aleksandr Chatrchyan, Majid Ekhterachian, Felix Kahlhoefer, Maciek Kierkla, William Lamb, and Alberto Roper Pol for useful discussions. TB and CT gratefully acknowledge support from the Alexander von Humboldt Foundation – via a Friedrich Wilhelm Bessel Award (TB) and a Feodor Lynen Research Fellowship (CT) – as well as through a FRIPRO grant of the Norwegian Research Council (project ID 353561 ‘DarkTurns’). This work is also funded by the Deutsche Forschungsgemeinschaft (DFG) through Germany’s Excellence Strategy — EXC 2121 “Quantum Universe” — 390833306 and through Grant No. 396021762 – TRR 257.

## A Details on the PTArcade likelihood

The PTArcade likelihood  $\ln \mathcal{L}_{\text{PTArcade}}$  is only valid for  $\ln \mathcal{L}_{\text{PTArcade}} \geq \tau \approx -110$  because it features unphysical plateaus below this value. For smaller values of  $\ln \mathcal{L}_{\text{PTArcade}}$ , we therefore use an approximate likelihood  $\mathcal{L}_{\text{approx}}$  that penalises parameter points which are too far away from the region of interest. This approximate likelihood is constructed to become maximal when the peak frequency and amplitude of the GW signal correspond to the region preferred by PTA data, cf. right panel of figure 1. We thus use a combined likelihood  $\mathcal{L}_{\text{PTA}}$  with

$$\begin{aligned}\ln \mathcal{L}_{\text{PTA}} &= \ln \mathcal{L}_{\text{PTArcade}} + \Theta(\tau - \ln \mathcal{L}_{\text{PTArcade}}) \times [\tau - \ln \mathcal{L}_{\text{PTArcade}} + \ln \mathcal{L}_{\text{approx}}] , \\ \ln \mathcal{L}_{\text{approx}} &= -(\log_{10}(h^2 \Omega_{\text{GW}}^{\text{peak}}) + 8.13)^2 - (\log_{10}(f_{\text{GW}}^{\text{peak}}/\text{Hz}) + 7.70)^2 ,\end{aligned}\quad (\text{A.1})$$

which ensures a smooth transition between both likelihoods. Using  $\mathcal{L}_{\text{PTA}}$  leads to a quicker convergence of the sampling algorithm than using  $\mathcal{L}_{\text{PTArcade}}$ , without compromising accuracy. The origin of the plateaus in the PTArcade likelihood is found in the `ceffyl` source code<sup>5</sup>, which sets the likelihood of a given element of the Bayesian spectrogram ('violin') to a constant value if the GW amplitude at that frequency is outside the prior range of the violin. Note further that the threshold parameter has a value of  $\tau \approx -110$  only in recent versions of `ceffyl` (starting from a normalisation fix introduced in September 2023) and consequently in PTArcade versions that correctly depend on these releases (in particular  $\text{PTArcade} \geq \text{v1.1.5}$ ). In earlier PTArcade versions (e.g. v1.1.1), one instead needs to use  $\tau = -55$ , due to an undocumented `tempo2` installation issue, which forced the use of an older `ceffyl` release. The installation issue has been resolved in later PTArcade releases, such that the more recent versions of PTArcade can now be used for a consistent Bayesian model comparison. The normalisation of the likelihood has no impact on parameter estimation or frequentist likelihood analyses, as performed in this work.

## B Effective potential for the flip-flop model

In this appendix we provide further details about the effective potential computation for the two-step transition model introduced in section 3.3. The tree-level potential in eq. (3.20) has four minima located at

$$\langle \phi \rangle_{1,2} = \begin{pmatrix} 0 \\ \pm v_2 \end{pmatrix} \equiv \begin{pmatrix} 0 \\ \pm v/\gamma \end{pmatrix} \quad \text{and} \quad \langle \phi \rangle_{3,4} = \begin{pmatrix} \pm v_1 \\ 0 \end{pmatrix} \equiv \begin{pmatrix} \pm \sqrt{1 + \lambda_1/\lambda_0} v \\ 0 \end{pmatrix} , \quad (\text{B.1})$$

at which the tree-level potential becomes

$$V_{\text{tree}}(0, \pm v_2) = 0 \quad \text{and} \quad V_{\text{tree}}(\pm v_1, 0) = -\frac{\lambda_1}{4} \left( 2 + \frac{\lambda_1}{\lambda_0} \right) v^4 . \quad (\text{B.2})$$

---

<sup>5</sup><https://github.com/astrolamb/ceffyl/blob/32f5b43cd8d6d1b3ee262c2a11f01eec64df34d5/ceffyl/Ceffyl.py#L505>

The background field-dependent mass matrix for the scalars reads

$$\mathcal{M}^2(\phi_1, \phi_2) = \begin{pmatrix} -v^2(\lambda_0 + \lambda_1) + 3\lambda_0\phi_1^2 + \phi_2^2(\gamma^2\lambda_0 + \lambda_{12}) & 2\phi_1\phi_2(\gamma^2\lambda_0 + \lambda_{12}) \\ 2\phi_1\phi_2(\gamma^2\lambda_0 + \lambda_{12}) & -\gamma^2\lambda_0v^2 + \phi_1^2(\gamma^2\lambda_0 + \lambda_{12}) + 3\gamma^4\lambda_0\phi_2^2 \end{pmatrix}. \quad (\text{B.3})$$

Since  $\lambda_0, \lambda_1 > 0$  and hence  $V_{\text{tree}}(\langle\phi\rangle_{3,4}) < V_{\text{tree}}(\langle\phi\rangle_{1,2})$ , the global minimum lies on the  $\phi_1$ -axis where the off-diagonal elements of  $\mathcal{M}$  vanish. Ignoring the impact of domain walls and in order to simplify the analysis (see discussion in section 3.3), we choose  $\langle\phi\rangle_3 = (+v_1, 0)$  as the vev in the broken phase after the transition.

In order to be able to use the vev as an input parameter for our numerical scan, we employ an on-shell-like scheme for renormalising the 1-loop effective potential, as introduced in ref. [75] for the study of phase transitions in multi-Higgs models. In doing so, the vev and the masses of the two dark singlet scalars are kept at their tree-level values after including the Coleman-Weinberg contribution to the potential. The counterterm potential therefore has the form

$$V_{\text{ct}} = -\frac{\delta\mu_1^2}{2}\phi_1^2 - \frac{\delta\mu_2^2}{2}\phi_2^2 + \frac{\delta\lambda_1}{4}\phi_1^4, \quad (\text{B.4})$$

where the counterterms are determined by the renormalisation conditions

$$\delta\lambda_1 = \frac{1}{2v_1^3} \frac{\partial V_{\text{CW}}}{\partial\phi_1} \Big|_{(v_1,0)} - \frac{1}{2v_1^2} \frac{\partial^2 V_{\text{CW}}}{\partial\phi_2^2} \Big|_{(v_1,0)}, \quad (\text{B.5})$$

$$\delta\mu_1^2 = \frac{3}{2v_1} \frac{\partial V_{\text{CW}}}{\partial\phi_2} \Big|_{(v_1,0)} - \frac{1}{2} \frac{\partial^2 V_{\text{CW}}}{\partial\phi_2^2} \Big|_{(v_1,0)}, \quad \text{and} \quad (\text{B.6})$$

$$\delta\mu_2^2 = \frac{\partial^2 V_{\text{CW}}}{\partial\phi_2^2} \Big|_{(v_1,0)}. \quad (\text{B.7})$$

To account for the resummation of daisy diagrams, we employ the Arnold-Espinosa method and add the thermal mass corrections [78]

$$\Pi_{\phi_1}(T) = \frac{T^2}{24} (y^2 + 2(3 + \gamma^2)\lambda_0 + \lambda_{12}) \quad \text{and} \quad \Pi_{\phi_2}(T) = \frac{T^2}{12} (\gamma^2\lambda_0 + 3\gamma^4\lambda_0 + \lambda_{12}) \quad (\text{B.8})$$

to the diagonal elements of the mass matrix in eq. (B.3) in the daisy contribution to the thermal potential, cf. eq. (3.11). We obtained these hard thermal masses by computing the thermal self-energy matrix  $\Pi(T) = \partial^2 V_T / (\partial\phi_i \partial\phi_j)$  to leading order in temperature and couplings.

## C Model parameter posterior distributions and benchmark points

In this appendix, we present posterior distributions ('triangle plots') of the model parameters, and the derived masses of the dark sector states after the phase transition, for the

Model	Parameter	Value
Abelian Higgs $U(1)'$	$\tilde{g}$	2.7829
	$\lambda$	0.0406
	$v/\text{GeV}$	0.24
Conformal $U(1)'$	$g$	0.692
	$v/\text{GeV}$	0.14
Flip-flop	$\lambda_0$	0.02432
	$\lambda_1$	0.014524
	$\lambda_{12}$	0.023401
	$v/\text{GeV}$	0.927
	$y$	1.0
	$\gamma$	1.0

**Table 2:** Benchmark parameter values for the three example models highlighted in the main text. We quote all significant digits obtained in the numerical analysis up to the degree of accuracy that is relevant for reproducing the PTA fit (cf. table 1 in the main text). For the derived model parameters, in particular the particle masses after the phase transition, see figures 10, 11, and 12.

Benchmark point	$\alpha$	$\beta/H$	$RH_*$	$T_{\text{nuc}}$ MeV	$T_p$ MeV	$T_{\text{reh}}$ MeV	$\ln \mathcal{L}_{\text{PTArcade}}$
Abelian dark Higgs	1.74	22.8	0.19	43.6	34.7	46.0	-103.21
Conformal $U(1)'$	821	57.9	0.08	3.16	2.58	14.5	-103.28
Flip-flop	0.70	5.5	0.80	285	173	192	-103.42

**Table 3:** Phase transition parameters for the three benchmark points given in table 2. The last column shows the log-likelihood values for the NANOGrav 15 yr data obtained using `PTArcade` v1.1.5.

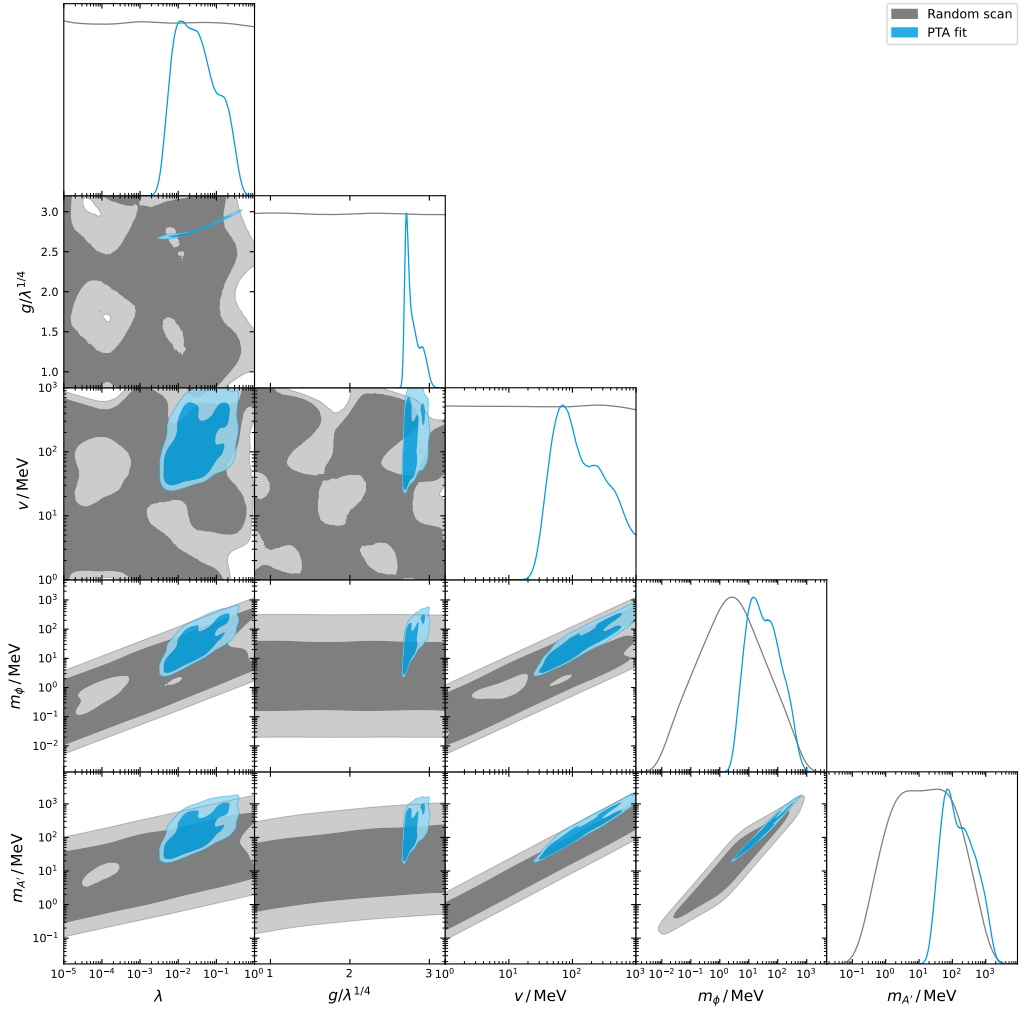
three models considered in the main text. In each case, we show the original random samples in grey, along with the preferred regions after sampling over the PTA likelihood in colour. We summarise our benchmark points, corresponding to the best-fit points of the latter scans, and their corresponding phase transition parameters in tables 2 and 3, respectively. We checked that the bubble wall velocity for all three models is  $v_w \simeq 1$  when using the LTE approximation for the friction [112].

Figure 10 shows the results of our random and `ultranest` scans over the Abelian dark Higgs model parameter space. The posterior of the coupling combination  $\tilde{g} = g/\lambda^{1/4}$  has a broad peak at  $\tilde{g} \simeq 2.5 - 3$ , which corresponds to the requirement of a sufficiently strong phase transition. For larger  $\tilde{g}$ , the transition becomes too strong and the GW amplitude overshoots the PTA data, eventually also leading to percolation problems due to excessive supercooling. Conversely, for smaller  $\tilde{g}$  the transition becomes too weak to explain the

PTA signal. The quartic coupling  $\lambda$  also has a broad distribution between  $10^{-3}$  and 1; note however that for each given  $\lambda$ , the value of  $\tilde{g}$  to obtain a good PTA fit needs to be tuned up to the fourth significant digit, cf. table 1. Correspondingly, the posterior distribution of the gauge coupling  $g = \tilde{g}\lambda^{1/4}$  (not shown in the plot) also has a broad distribution ranging from 0.5 to 2.5. The resulting mass distributions of the dark Higgs and dark gauge boson peak around  $m_\phi \sim 10$  MeV and  $m_{A'} \sim 100$  MeV, each with tails spanning one order of magnitude in mass. The vev  $v$  is the least constrained parameter, peaking at  $\sim 100$  MeV. The dominant effect of a specific vev on the GW signal is to set the scale of the peak frequency, thus resulting only in a very mild degree of tuning of this parameter for a fixed set of couplings. Correspondingly, the posterior distribution of  $v$  is rather flat, consistent with the discussion in section 3.2. We note that it is mostly the left shoulder of the distribution in  $v$  that is directly driven by data, coming from the requirement that the peak of the spectrum must not be located at frequencies  $f \ll 10^{-8}$  Hz, cf. figure 1. The fact that larger values of  $v$  are disfavoured, in contrast, is a consequence of an increasing difficulty to achieve sufficiently low  $\beta/H$  (needed to maintain the required overall amplitude). As long as the data themselves do not show clear evidence for a peak structure, let alone its exact location, the upper bound on the  $v$  distribution is thus more a model limitation than something that can be inferred from the data. Note that the cutoff of the posterior distribution at the upper prior boundary also contributes to the mild cut-off in the mass distributions visible in  $m_{A'}$ .

Next, figure 11 shows our results for the flip-flop model with a two-step phase transition. Here the vev  $v$  is again the least constrained parameter, centred around  $v \sim 1$  GeV and thus at a considerably larger value than for the other models (see also figure 9). Note that we imposed  $y = \gamma = 1$  in order to simplify the numerical analysis when fitting the PTA signal; relaxing this assumption would likely broaden the preferred range of  $v$  even further. The quartic couplings  $\lambda_1$  and  $\lambda_{12}$  are as discussed in the main text highly tuned to  $\mathcal{O}(10^{-2})$  values, featuring very narrow posterior distributions. The quartic coupling  $\lambda_0$ , dictating the overall shape of the potential, is larger and generally less constrained (though still strongly peaked at its central value – which is however likely a sampling effect, see above). The total number of sampled points that yield a good fit to the PTA data, particularly visible in the panels with  $\lambda_0$  on the axes, is significantly smaller than for the other two models, indicating the numerical challenges in identifying parameter points yielding sufficiently slow phase transition in this model. The imposed mass cuts of both dark scalars to be above the muon threshold after the transition,  $m_{\phi_i} > 211$  MeV, is clearly visible in their mass distributions, which peak between 300 MeV and 1 GeV, with slightly larger  $m_{\phi_1}$  than  $m_{\phi_2}$  in general. The fermion is typically the heaviest dark sector state, with a mass sharply peaking at around  $m_\psi \simeq 1$  GeV, thus safely avoiding BBN constraints via its Boltzmann suppression prior to the decay of the dark scalars.

In figure 12, finally, we display the results for the conformal model. We find that the preferred value of the dark Higgs vev after the transition lies around  $v \simeq 200$  MeV, though at  $2\sigma$  a range of  $80$  MeV  $\lesssim v \lesssim 400$  MeV is allowed. The dark gauge coupling is more strongly constrained, peaking around  $g \simeq 0.6 - 0.7$  in accordance with the results presented in ref. [55]. This implies that the resulting masses of the dark Higgs and dark gauge boson



**Figure 10:** Triangle plot showing the preferred regions of the Abelian dark Higgs model after sampling over the PTA likelihood. The random samples are shown in grey.

typically lie in the range of a few tens of MeV and around 100 MeV, respectively.

## References

- [1] **LIGO Scientific, Virgo Collaboration**, B. P. Abbott et al., *Observation of Gravitational Waves from a Binary Black Hole Merger*, *Phys. Rev. Lett.* **116** (2016), no. 6 061102, [[1602.03837](https://arxiv.org/abs/1602.03837)].
- [2] **LISA Collaboration**, P. Amaro-Seoane et al., *Laser Interferometer Space Antenna*, [[1702.00786](https://arxiv.org/abs/1702.00786)].
- [3] **NANOGrav Collaboration**, Z. Arzoumanian et al., *The NANOGrav 12.5 yr Data Set: Search for an Isotropic Stochastic Gravitational-wave Background*, *Astrophys. J. Lett.* **905** (2020), no. 2 L34, [[2009.04496](https://arxiv.org/abs/2009.04496)].

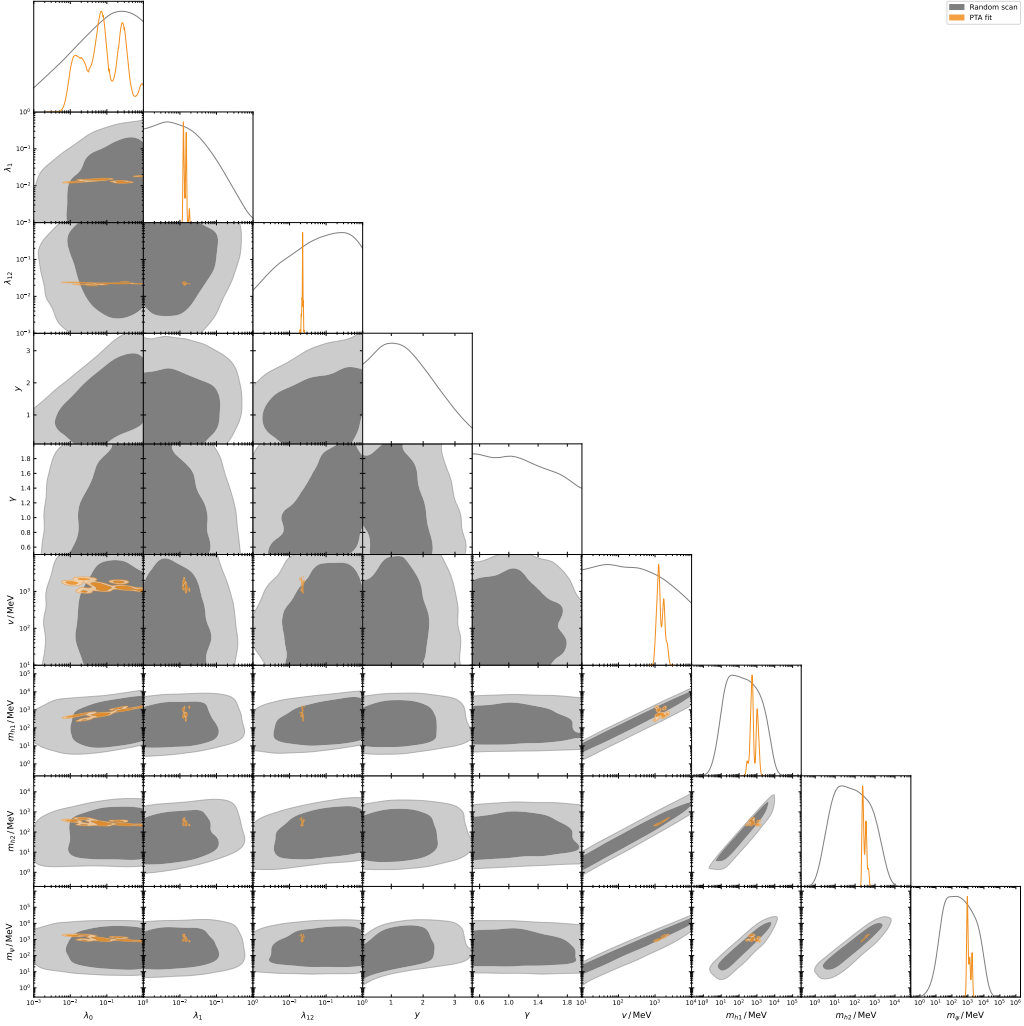


**Figure 11:** Triangle plot showing the preferred regions of the flip-flop model after sampling over the PTA likelihood and imposing the mass cuts on the dark singlets. The random samples are shown in grey. Note that the couplings  $y$  and  $\gamma$  have been fixed to unity for the PTA fit (indicated by missing posterior distributions in the respective panels) and that the posteriors in the  $\lambda_0$  direction are rather poorly sampled due to numerical challenges in achieving a sufficiently slow phase transition.

- [4] **NANOGrav Collaboration**, G. Agazie et al., *The NANOGrav 15-year Data Set: Evidence for a Gravitational-Wave Background*, *Astrophys. J. Lett.* **951** (2023), no. 1 [[2306.16213](#)].
- [5] J. Antoniadis et al., *The second data release from the European Pulsar Timing Array III. Search for gravitational wave signals*, [2306.16214](#).
- [6] D. J. Reardon et al., *Search for an isotropic gravitational-wave background with the Parkes Pulsar Timing Array*, *Astrophys. J. Lett.* **951** (2023), no. 1 [[2306.16215](#)].
- [7] H. Xu et al., *Searching for the Nano-Hertz Stochastic Gravitational Wave Background with the Chinese Pulsar Timing Array Data Release I*, *Res. Astron. Astrophys.* **23** (2023), no. 7

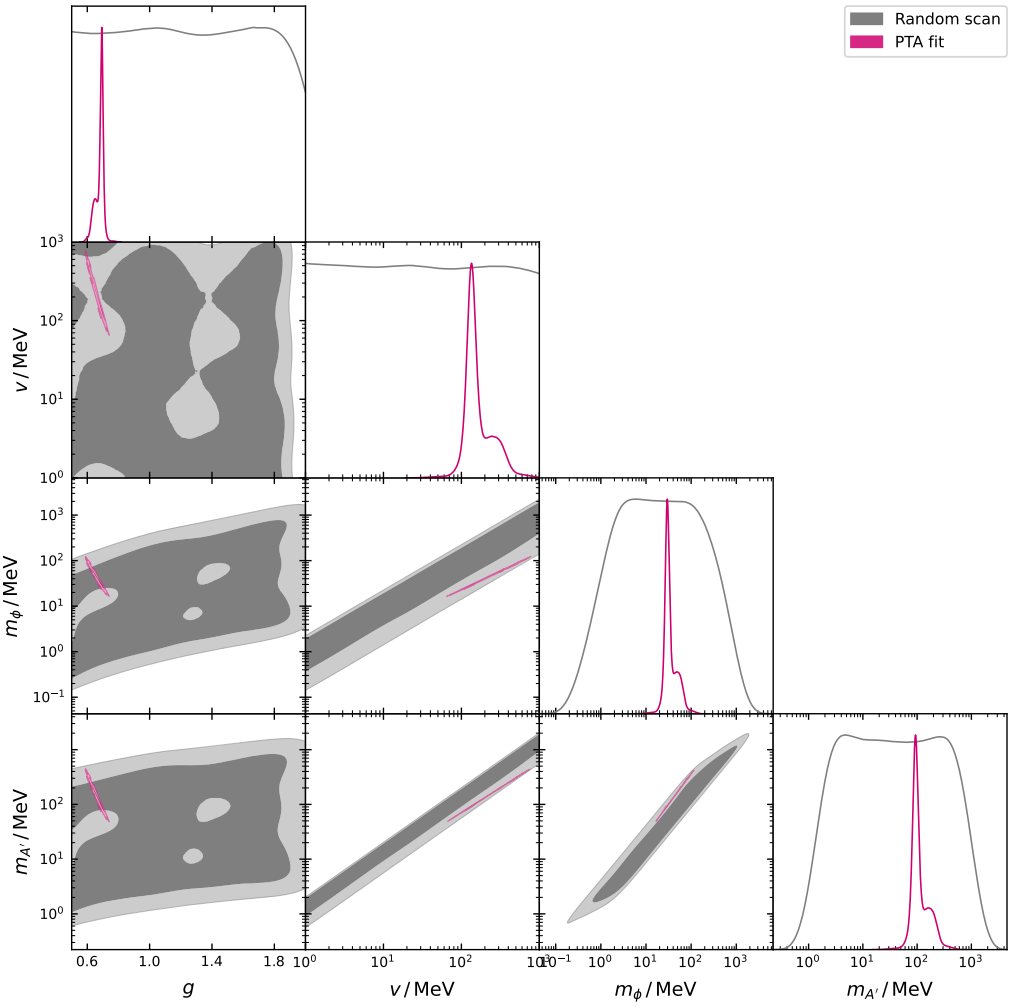


**Figure 12:** Triangle plot showing the preferred regions of the conformal model after sampling over the PTA likelihood. The random samples are shown in grey.

075024, [\[2306.16216\]](#).

[8] M. T. Miles et al., *The MeerKAT Pulsar Timing Array: the first search for gravitational waves with the MeerKAT radio telescope*, *Mon. Not. Roy. Astron. Soc.* **536** (2024), no. 2 1489–1500, [\[2412.01153\]](#).

[9] R. W. Hellings and G. W. Downs, *Upper limits on the isotropic gravitational radiation background from pulsar timing analysis.*, *Astrophys. J. Lett.* **265** (1983) L39–L42.

[10] **International Pulsar Timing Array Collaboration**, G. Agazie et al., *Comparing Recent Pulsar Timing Array Results on the Nanohertz Stochastic Gravitational-wave Background*, *Astrophys. J.* **966** (2024), no. 1 105, [\[2309.00693\]](#).

[11] W.-W. Yu and B. Allen, *Stochastic gravitational-wave background search using data from five pulsar timing arrays*, [\[2512.08666\]](#).

[12] J. A. Casey-Clyde, C. M. F. Mingarelli, J. E. Greene, K. Pardo, M. Nañez, et al., [A](#)

*Quasar-based Supermassive Black Hole Binary Population Model: Implications for the Gravitational Wave Background,* *Astrophys. J.* **924** (2022), no. 2 93, [[2107.11390](#)].

[13] L. Z. Kelley, L. Blecha, and L. Hernquist, *Massive Black Hole Binary Mergers in Dynamical Galactic Environments,* *Mon. Not. Roy. Astron. Soc.* **464** (2017), no. 3 3131–3157, [[1606.01900](#)].

[14] L. Z. Kelley, L. Blecha, L. Hernquist, A. Sesana, and S. R. Taylor, *The Gravitational Wave Background from Massive Black Hole Binaries in Illustris: spectral features and time to detection with pulsar timing arrays,* *Mon. Not. Roy. Astron. Soc.* **471** (2017), no. 4 4508–4526, [[1702.02180](#)].

[15] **NANOGrav Collaboration**, G. Agazie et al., *The NANOGrav 15 yr Data Set: Constraints on Supermassive Black Hole Binaries from the Gravitational-wave Background,* *Astrophys. J. Lett.* **952** (2023), no. 2 L37, [[2306.16220](#)].

[16] N. Chen, T. Di Matteo, Y. Zhou, L. Z. Kelley, L. Blecha, et al., *The Gravitational-wave Background from Massive Black Holes in the ASTRID Simulation,* *Astrophys. J. Lett.* **991** (2025), no. 1 L19, [[2502.01024](#)].

[17] G. Agazie et al., *The NANOGrav 15 yr Data Set: Piecewise Power-Law Reconstruction of the Gravitational-Wave Background,* [2601.09481](#).

[18] M. Milosavljevic and D. Merritt, *The Final parsec problem,* *AIP Conf. Proc.* **686** (2003), no. 1 201–210, [[astro-ph/0212270](#)].

[19] M. Chiaberge et al., *A recoiling supermassive black hole in a powerful quasar,* [2501.18730](#).

[20] **NANOGrav Collaboration**, A. Afzal et al., *The NANOGrav 15 yr Data Set: Search for Signals from New Physics,* *Astrophys. J. Lett.* **951** (2023), no. 1 L11, [[2306.16219](#)]. [Erratum: *Astrophys.J.Lett.* 971, L27 (2024)].

[21] S. Vagnozzi, *Implications of the NANOGrav results for inflation,* *Mon. Not. Roy. Astron. Soc.* **502** (2021), no. 1 L11–L15, [[2009.13432](#)].

[22] S. Blasi, V. Brdar, and K. Schmitz, *Has NANOGrav found first evidence for cosmic strings?,* *Phys. Rev. Lett.* **126** (2021), no. 4 041305, [[2009.06607](#)].

[23] J. Ellis and M. Lewicki, *Cosmic String Interpretation of NANOGrav Pulsar Timing Data,* *Phys. Rev. Lett.* **126** (2021), no. 4 041304, [[2009.06555](#)].

[24] W. Buchmuller, V. Domcke, and K. Schmitz, *From NANOGrav to LIGO with metastable cosmic strings,* *Phys. Lett. B* **811** (2020) 135914, [[2009.10649](#)].

[25] R. Samanta and S. Datta, *Gravitational wave complementarity and impact of NANOGrav data on gravitational leptogenesis,* *JHEP* **05** (2021) 211, [[2009.13452](#)].

[26] S.-Y. Guo, M. Khlopov, X. Liu, L. Wu, Y. Wu, et al., *Footprints of axion-like particle in pulsar timing array data and James Webb Space Telescope observations,* *Sci. China Phys. Mech. Astron.* **67** (2024), no. 11 111011, [[2306.17022](#)].

[27] S. F. King, D. Marfatia, and M. H. Rahat, *Toward distinguishing Dirac from Majorana neutrino mass with gravitational waves,* *Phys. Rev. D* **109** (2024), no. 3 035014, [[2306.05389](#)].

[28] P. F. Depta, K. Schmidt-Hoberg, P. Schwaller, and C. Tasillo, *Signals of merging supermassive black holes in pulsar timing arrays,* *Phys. Rev. Res.* **7** (2025), no. 1 013196, [[2306.17836](#)].

[29] V. De Luca, G. Franciolini, and A. Riotto, *NANOGrav Data Hints at Primordial Black Holes as Dark Matter*, *Phys. Rev. Lett.* **126** (2021), no. 4 041303, [[2009.08268](#)].

[30] V. Vaskonen and H. Veermäe, *Did NANOGrav see a signal from primordial black hole formation?*, *Phys. Rev. Lett.* **126** (2021), no. 5 051303, [[2009.07832](#)].

[31] K. Kohri and T. Terada, *Solar-Mass Primordial Black Holes Explain NANOGrav Hint of Gravitational Waves*, *Phys. Lett. B* **813** (2021) 136040, [[2009.11853](#)].

[32] C. Ünal, E. D. Kovetz, and S. P. Patil, *Multimessenger probes of inflationary fluctuations and primordial black holes*, *Phys. Rev. D* **103** (2021), no. 6 063519, [[2008.11184](#)].

[33] A. Ashoorioon, K. Rezazadeh, and A. Rostami, *NANOGrav signal from the end of inflation and the LIGO mass and heavier primordial black holes*, *Phys. Lett. B* **835** (2022) 137542, [[2202.01131](#)].

[34] Y. Nakai, M. Suzuki, F. Takahashi, and M. Yamada, *Gravitational Waves and Dark Radiation from Dark Phase Transition: Connecting NANOGrav Pulsar Timing Data and Hubble Tension*, *Phys. Lett. B* **816** (2021) 136238, [[2009.09754](#)].

[35] W. Ratzinger and P. Schwaller, *Whispers from the dark side: Confronting light new physics with NANOGrav data*, *SciPost Phys.* **10** (2021), no. 2 047, [[2009.11875](#)].

[36] **NANOGrav Collaboration**, Z. Arzoumanian et al., *Searching for Gravitational Waves from Cosmological Phase Transitions with the NANOGrav 12.5-Year Dataset*, *Phys. Rev. Lett.* **127** (2021), no. 25 251302, [[2104.13930](#)].

[37] T. Bringmann, P. F. Depta, T. Konstandin, K. Schmidt-Hoberg, and C. Tasillo, *Does NANOGrav observe a dark sector phase transition?*, *JCAP* **11** (2023) 053, [[2306.09411](#)].

[38] E. Madge, E. Morgante, C. Puchades-Ibáñez, N. Ramberg, W. Ratzinger, et al., *Primordial gravitational waves in the nano-Hertz regime and PTA data — towards solving the GW inverse problem*, *JHEP* **10** (2023) 171, [[2306.14856](#)].

[39] J. Gonçalves, D. Marfatia, A. P. Morais, and R. Pasechnik, *Supercooled phase transitions in conformal dark sectors explain NANOGrav data*, *Phys. Lett. B* **869** (2025) 139829, [[2501.11619](#)].

[40] S. Gori et al., *Dark Sector Physics at High-Intensity Experiments*, [2209.04671](#).

[41] **Planck Collaboration**, N. Aghanim et al., *Planck 2018 results. VI. Cosmological parameters*, *Astron. Astrophys.* **641** (2020) A6, [[1807.06209](#)]. [Erratum: *Astron. Astrophys.* **652**, C4 (2021)].

[42] T.-H. Yeh, J. Shelton, K. A. Olive, and B. D. Fields, *Probing physics beyond the standard model: limits from BBN and the CMB independently and combined*, *JCAP* **10** (2022) 046, [[2207.13133](#)].

[43] H. Bagherian, M. Ekhterachian, and S. Stelzl, *The bearable inhomogeneity of the baryon asymmetry*, *JHEP* **01** (2026) 068, [[2505.15904](#)].

[44] M. Hufnagel, K. Schmidt-Hoberg, and S. Wild, *BBN constraints on MeV-scale dark sectors. Part II. Electromagnetic decays*, *JCAP* **11** (2018) 032, [[1808.09324](#)].

[45] L. Forestell, D. E. Morrissey, and G. White, *Limits from BBN on Light Electromagnetic Decays*, *JHEP* **01** (2019) 074, [[1809.01179](#)].

[46] P. F. Depta, M. Hufnagel, and K. Schmidt-Hoberg, *Updated BBN constraints on electromagnetic decays of MeV-scale particles*, *JCAP* **04** (2021) 011, [[2011.06519](#)].

[47] P. F. Depta, M. Hufnagel, and K. Schmidt-Hoberg, *ACROPOLIS: A generiC fRamework fOr Photodisintegration Of Light elements*, *JCAP* **03** (2021) 061, [[2011.06518](#)].

[48] M. Kawasaki, K. Kohri, T. Moroi, K. Murai, and H. Murayama, *Big-bang nucleosynthesis with sub-GeV massive decaying particles*, *JCAP* **12** (2020) 048, [[2006.14803](#)].

[49] **LISA Cosmology Working Group Collaboration**, C. Caprini, R. Jinno, M. Lewicki, E. Madge, M. Merchand, et al., *Gravitational waves from first-order phase transitions in LISA: reconstruction pipeline and physics interpretation*, *JCAP* **10** (2024) 020, [[2403.03723](#)].

[50] R. Jinno, T. Konstandin, H. Rubira, and I. Stomberg, *Higgsless simulations of cosmological phase transitions and gravitational waves*, *JCAP* **02** (2023) 011, [[2209.04369](#)].

[51] C. Caprini, R. Jinno, T. Konstandin, A. Roper Pol, H. Rubira, et al., *Gravitational waves from first-order phase transitions: from weak to strong*, *JHEP* **07** (2025) 217, [[2409.03651](#)].

[52] J. Matuszak and C. Tasillo, *TransitionListener v2.0 – Towards precision calculations in cosmological phase transitions*, [2603.XXXX](#).

[53] A. Megevand and S. Ramirez, *Bubble nucleation and growth in very strong cosmological phase transitions*, *Nucl. Phys. B* **919** (2017) 74–109, [[1611.05853](#)].

[54] J. R. Espinosa, T. Konstandin, J. M. No, and G. Servant, *Energy Budget of Cosmological First-order Phase Transitions*, *JCAP* **06** (2010) 028, [[1004.4187](#)].

[55] S. Balan, T. Bringmann, F. Kahlhoefer, J. Matuszak, and C. Tasillo, *Sub-GeV dark matter and nano-Hertz gravitational waves from a classically conformal dark sector*, *JCAP* **08** (2025) 062, [[2502.19478](#)].

[56] A. Mitridate, D. Wright, R. von Eckardstein, T. Schröder, J. Nay, et al., *PTArcade*, [2306.16377](#).

[57] I. Baldes and C. Garcia-Cely, *Strong gravitational radiation from a simple dark matter model*, *JHEP* **05** (2019) 190, [[1809.01198](#)].

[58] N. Levi, T. Opferkuch, and D. Redigolo, *The supercooling window at weak and strong coupling*, *JHEP* **02** (2023) 125, [[2212.08085](#)].

[59] Y. Gouttenoire, *Primordial black holes from conformal Higgs*, *Phys. Lett. B* **855** (2024) 138800, [[2311.13640](#)].

[60] K. Fujikura, S. Girmohanta, Y. Nakai, and M. Suzuki, *NANOGrav signal from a dark conformal phase transition*, *Phys. Lett. B* **846** (2023) 138203, [[2306.17086](#)].

[61] M. Hosseini, S. Yaser Ayazi, and A. Mohamadnejad, *Gravitational wave effects and phenomenology of a two-component dark matter model*, *Eur. Phys. J. C* **84** (2024), no. 5 485, [[2308.00395](#)].

[62] A. Salvio, *Pulsar timing arrays and primordial black holes from a supercooled phase transition*, *Phys. Lett. B* **852** (2024) 138639, [[2312.04628](#)].

[63] F. Ertas, F. Kahlhoefer, and C. Tasillo, *Turn up the volume: listening to phase transitions in hot dark sectors*, *JCAP* **02** (2022), no. 02 014, [[2109.06208](#)].

[64] F. Giese, T. Konstandin, K. Schmitz, and J. van de Vis, *Model-independent energy budget for LISA*, *JCAP* **01** (2021) 072, [[2010.09744](#)].

[65] F. Giese, T. Konstandin, and J. van de Vis, *Model-independent energy budget of cosmological first-order phase transitions—A sound argument to go beyond the bag model*, *JCAP* **07** (2020), no. 07 057, [[2004.06995](#)].

[66] P. Athron, C. Balázs, A. Fowlie, L. Morris, and L. Wu, *Cosmological phase transitions: From perturbative particle physics to gravitational waves*, *Prog. Part. Nucl. Phys.* **135** (2024) 104094, [[2305.02357](#)].

[67] J. Ellis, M. Lewicki, and J. M. No, *On the Maximal Strength of a First-Order Electroweak Phase Transition and its Gravitational Wave Signal*, *JCAP* **04** (2019) 003, [[1809.08242](#)].

[68] G. H. Derrick, *Comments on nonlinear wave equations as models for elementary particles*, *J. Math. Phys.* **5** (1964) 1252–1254.

[69] S. Coleman, *Aspects of Symmetry: Selected Erice Lectures*. Cambridge University Press, Cambridge, U.K., 1985.

[70] C. Caprini et al., *Detecting gravitational waves from cosmological phase transitions with LISA: an update*, *JCAP* **03** (2020) 024, [[1910.13125](#)].

[71] K. Kajantie, M. Laine, K. Rummukainen, and M. E. Shaposhnikov, *Generic rules for high temperature dimensional reduction and their application to the standard model*, *Nucl. Phys. B* **458** (1996) 90–136, [[hep-ph/9508379](#)].

[72] D. Croon, O. Gould, P. Schicho, T. V. I. Tenkanen, and G. White, *Theoretical uncertainties for cosmological first-order phase transitions*, *JHEP* **04** (2021) 055, [[2009.10080](#)].

[73] M. Lewicki, M. Merchand, L. Sagunski, P. Schicho, and D. Schmitt, *Impact of theoretical uncertainties on model parameter reconstruction from GW signals sourced by cosmological phase transitions*, *Phys. Rev. D* **110** (2024), no. 2 023538, [[2403.03769](#)].

[74] S. R. Coleman and E. J. Weinberg, *Radiative Corrections as the Origin of Spontaneous Symmetry Breaking*, *Phys. Rev. D* **7** (1973) 1888–1910.

[75] P. Basler and M. Mühlleitner, *BSMPT (Beyond the Standard Model Phase Transitions): A tool for the electroweak phase transition in extended Higgs sectors*, *Comput. Phys. Commun.* **237** (2019) 62–85, [[1803.02846](#)].

[76] M. Quiros, *Finite temperature field theory and phase transitions*, in *ICTP Summer School in High-Energy Physics and Cosmology*, pp. 187–259, 1, 1999. [hep-ph/9901312](#).

[77] M. E. Carrington, *The Effective potential at finite temperature in the Standard Model*, *Phys. Rev. D* **45** (1992) 2933–2944.

[78] P. B. Arnold and O. Espinosa, *The Effective potential and first order phase transitions: Beyond leading-order*, *Phys. Rev. D* **47** (1993) 3546, [[hep-ph/9212235](#)]. [Erratum: *Phys. Rev. D* 50, 6662 (1994)].

[79] T. Bringmann, T. E. Gonzalo, F. Kahlhoefer, J. Matuszak, and C. Tasillo, *Hunting WIMPs with LISA: correlating dark matter and gravitational wave signals*, *JCAP* **05** (2024) 065, [[2311.06346](#)].

[80] F. Costa, J. Hoefken Zink, M. Lucente, S. Pascoli, and S. Rosauro-Alcaraz, *Supercooled dark scalar phase transitions explanation of NANOGrav data*, *Phys. Lett. B* **868** (2025) 139634, [[2501.15649](#)].

[81] J. H. Chang, R. Essig, and S. D. McDermott, *Revisiting Supernova 1987A Constraints on Dark Photons*, *JHEP* **01** (2017) 107, [[1611.03864](#)].

[82] A. Caputo, H.-T. Janka, G. Raffelt, and S. Yun, *Cooling the Shock: New Supernova Constraints on Dark Photons*, *Phys. Rev. Lett.* **134** (2025), no. 15 151002, [[2502.01731](#)].

[83] T. Ferber, C. Garcia-Cely, and K. Schmidt-Hoberg, *BelleII sensitivity to long-lived dark photons*, *Phys. Lett. B* **833** (2022) 137373, [[2202.03452](#)].

[84] **NA64 Collaboration**, S. Gninenko, *Proposal for an experiment to search for dark sector particles weakly coupled to muon at the SPS*, tech. rep., CERN, Geneva, 2019.

[85] **LHCb Collaboration**, *Future physics potential of LHCb*, [LHCb-PUB-2022-012](#), [CERN-LHCb-PUB-2022-012](#).

[86] L. A. Anchordoqui et al., *The Forward Physics Facility: Sites, experiments, and physics potential*, *Phys. Rept.* **968** (2022) 1–50, [[2109.10905](#)].

[87] A. Apyan et al., *DarkQuest: A dark sector upgrade to SpinQuest at the 120 GeV Fermilab Main Injector*, in *Snowmass 2021*, 3, 2022. [2203.08322](#).

[88] C. Ahdida et al., *Post-LS3 Experimental Options in ECN3*, [2310.17726](#).

[89] A. Fradette, M. Pospelov, J. Pradler, and A. Ritz, *Cosmological beam dump: constraints on dark scalars mixed with the Higgs boson*, *Phys. Rev. D* **99** (2019), no. 7 075004, [[1812.07585](#)].

[90] **NA62 Collaboration**, E. Cortina Gil et al., *Measurement of the very rare  $K^+ \rightarrow \pi^+ \nu \bar{\nu}$  decay*, *JHEP* **06** (2021) 093, [[2103.15389](#)].

[91] M. Kierkla, B. Swiezewska, T. V. I. Tenkanen, and J. van de Vis, *Gravitational waves from supercooled phase transitions: dimensional transmutation meets dimensional reduction*, *JHEP* **02** (2024) 234, [[2312.12413](#)].

[92] J. Buchner, *UltraNest - a robust, general purpose Bayesian inference engine*, *The Journal of Open Source Software* **6** (Apr., 2021) 3001, [[2101.09604](#)].

[93] M. Lewicki and V. Vaskonen, *Impact of cosmic expansion on gravitational wave spectra from strongly supercooled first-order phase transitions*, [2511.15687](#).

[94] H. Kodama, M. Sasaki, and K. Sato, *Abundance of Primordial Holes Produced by Cosmological First Order Phase Transition*, *Prog. Theor. Phys.* **68** (1982) 1979.

[95] M. Lewicki, P. Toczek, and V. Vaskonen, *Primordial black holes from strong first-order phase transitions*, *JHEP* **09** (2023) 092, [[2305.04924](#)].

[96] Y. Gouttenoire and T. Volansky, *Primordial black holes from supercooled phase transitions*, *Phys. Rev. D* **110** (2024), no. 4 043514, [[2305.04942](#)].

[97] G. Franciolini, Y. Gouttenoire, and R. Jinno, *Curvature Perturbations from First-Order Phase Transitions: Implications to Black Holes and Gravitational Waves*, [2503.01962](#).

[98] X. Wang, C. Balázs, R. Ding, and C. Tian, *How large are curvature perturbations from slow first-order phase transitions? A gauge-invariant analysis*, [2601.14412](#).

[99] M. Lewicki and V. Vaskonen, *Gravitational waves from bubble collisions and fluid motion in strongly supercooled phase transitions*, *Eur. Phys. J. C* **83** (2023), no. 2 109, [[2208.11697](#)].

[100] M. Yamada, *Maximal GW amplitude from bubble collisions in supercooled phase transitions*, [2509.13402](#).

[101] A. Chatrchyan, M. C. D. Marsh, and C. Nikolis, *Gravitational waves from a dilaton-induced, first-order QCD phase transition*, [2507.01191](#).

- [102] K. Freese and M. W. Winkler, *Have pulsar timing arrays detected the hot big bang: Gravitational waves from strong first order phase transitions in the early Universe*, *Phys. Rev. D* **106** (2022), no. 10 103523, [[2208.03330](#)].
- [103] S. Blasi and A. Mariotti, *Domain Walls Seeding the Electroweak Phase Transition*, *Phys. Rev. Lett.* **129** (2022), no. 26 261303, [[2203.16450](#)].
- [104] S. Blasi, R. Jinno, T. Konstandin, H. Rubira, and I. Stomberg, *Gravitational waves from defect-driven phase transitions: domain walls*, *JCAP* **10** (2023) 051, [[2302.06952](#)].
- [105] P. Agrawal, S. Blasi, A. Mariotti, and M. Nee, *Electroweak phase transition with a double well done doubly well*, *JHEP* **06** (2024) 089, [[2312.06749](#)].
- [106] A. Chatrchyan, F. Niedermann, and P. Richman-Taylor, *String-induced vacuum decay*, [2510.27579](#).
- [107] Y. Bai, Y. Xu, and Y. Yang, *Heterogeneous Cosmological Phase Transitions: Seeded by Domain Walls and Junctions*, [2512.10917](#).
- [108] P. Agrawal, G. R. Kane, V. Loladze, and M. Reig, *Supercooled confinement*, *JHEP* **10** (2025) 066, [[2504.00199](#)].
- [109] I. Garcia Garcia, R. Lasenby, and J. March-Russell, *Twin Higgs WIMP Dark Matter*, *Phys. Rev. D* **92** (2015), no. 5 055034, [[1505.07109](#)].
- [110] T. Konstandin, A.-M. Lemke, A. Mitridate, and E. Perboni, *The impact of cosmic variance on PTAs anisotropy searches*, *JCAP* **04** (2025) 059, [[2408.07741](#)].
- [111] T. Konstandin, A.-M. Lemke, A. Mitridate, and E. Perboni, *Prospects and Limitations of PTAs Anisotropy Searches – The Frequentist Case*, [2509.07074](#).
- [112] W.-Y. Ai, B. Laurent, and J. van de Vis, *Model-independent bubble wall velocities in local thermal equilibrium*, *JCAP* **07** (2023) 002, [[2303.10171](#)].